1949

Investigation of noisy character of thermally and stress induced phase transformations by acoustic emission in $Ni_{49}Fe_{18}Ga_{27}Co_6$ shape memory single crystals

Thesis for the Degree of Doctor of Philosophy (PhD)

Sarah Mahmoud Mohamed Kamel

Supervisor:

Prof. Dr. Dezső L. Beke

UNIVERSITY OF DEBRECEN

Doctoral Council of Natural Sciences and Information Technology

Doctoral School of Physics

Debrecen, 2024

Hereby I declare that I prepared this thesis within the Doctoral Council of Natural Sciences and Information Technology, Doctoral School of Physic, University of Debrecen in order to obtain a PhD Degree in Natural Sciences at Debrecen University.

The results published in the thesis are not reported in any other PhD theses.

Debrecen, 2024 . . . .

Sarah Mahmoud Mohamed Kamel
candidate

Hereby I confirm that Sarah Mahmoud Mohamed Kamel candidate conducted her studies with my supervision within the Solid-State Physics and Material Science Doctoral Program of the Doctoral School of Physics between 2020 and 2024. The independent studies and research work of the candidate significantly contributed to the results published in the thesis.

I also declare that the results published in the thesis are not reported in any other thesis.

I support the acceptance of the thesis.

Debrecen, 2024 . . . . . .

.....

Prof. Dr. Dezső L. Beke
Supervisor

Investigation of noisy character of thermally and stress induced phase transformations by acoustic emission in $Ni_{49}Fe_{18}Ga_{27}Co_6$ shape memory single crystals

Dissertation submitted in partial fulfilment of the requirements for the doctoral (PhD) degree in **Physics**

Written by **Sarah Mahmoud Mohamed Kamel** certified MSc of Physics

Prepared in the framework of the Doctoral School of Physics of the University of Debrecen

Solid State Physics and Material Science programme

Dissertation advisor: **Prof. Dr. Dezső L. Beke**

The official opponents of the dissertation:

Dr. ....

Dr. ....

The evaluation committee:

Chairperson: Dr. ....

Members: Dr. ....

Dr. ....

Dr. ....

Dr. ....

The date of the dissertation defence: 202 .....

Table of content

List of symbols

List of the most important symbols

SMA	Shape Memory Alloy
$\boldsymbol{\sigma}$	Stress
T	Temperature
$\mathbb{B}$	Magnetic field
$\mathbb{E}$	Electric field
MT	Martensitic transformation
A	Austenite phase
M	Martensite phase
A/M	Austenite to martensite interface
SCs	Structural changes
A	Amplitude of an avalanche
D	Duration of an avalanche
S	Size of an avalanche
E	Energy of an avalanche
V(t)	Detected voltage
AE	Acoustic Emission
MFT	Mean field theory
A→M	Austenite to martensite transformation
M→A	Martensite to austenite transformation
ε	Engineering strain
TWSME	Two-Way shape Memory Alloy
SIM-aging	Stress-Induced Martensitic stabilization
G	Gibb's free energy
g	Gibb's free energy per unit volume

V	Volume
v_M	Volume of martensite
v_A	Volume of austenite
ξ	Martensite volume fraction
$\Delta g^{\downarrow}$	Total change of Gibb's free energy per unit volume for A→ M
$\Delta g^{c\downarrow}$	Chemical Gibb's free energy per unit volume for A→ M
$\mathcal{D}^{\downarrow}$	Dissipative energy per unit volume for A→ M
g^A	Chemical Gibb's free energy per unit volume of Austenite
g^M	Chemical Gibb's free energy per unit volume of Martensite
$\varepsilon^{tr\downarrow}$	Transformation strain for A→ M
$\varepsilon^{tr\uparrow}$	Transformation strain for M→ A
$\Delta u^{\downarrow}$	Change in internal energy per unit volume for A→ M
$\Delta u^{\uparrow}$	Change in internal energy per unit volume for M→ A
$\Delta s^{\downarrow}$	Change in entropy energy per unit volume for A→ M
$\Delta s^{\uparrow}$	Change in entropy energy per unit volume for M→ A
$E^{\downarrow}$	Elastic energy per unit volume for A→ M
$E^{\uparrow}$	Elastic energy per unit volume for M→ A
$\mathcal{D}$	Dissipative energy per unit volume
$\mathcal{D}_n$	Dissipative energy per unit volume for nucleation
$\mathcal{D}_f$	Dissipative energy per unit volume for friction
u^A	Energy per unit volume for A phase
u^M	Energy per unit volume for M phase
s^A	Entropy per unit volume for A phase
s^M	Entropy per unit volume for M phase
T_0	Equilibrium transformation temperature at σ = 0
σ_0	Equilibrium transformation stress at T = 0

M_s	Martensitic start temperature
M_f	Martensitic finish temperature
A_s	Austenite start temperature
A_f	Austenite finish temperature
σ_{M_s}	Martensitic start stress
σ_{M_f}	Martensitic finish stress
σ_{A_s}	Austenite start stress
σ_{A_f}	Austenite finish stress
d(ξ)	Derivative of chemical dissipative energy by ξ
e(ξ)	Derivative of chemical elastic energy by ξ
P(x)	Probability density function of x (which can be e.g. the energy, amplitude, duration time, area)
C	Normalization constant
x_c	Cut-off value
μ	Critical exponent
$\boldsymbol{\tau}$	Critical exponent for area PDF
$\boldsymbol{\varepsilon}$	Critical exponent for energy PDF
$\boldsymbol{\alpha}$	Critical exponent for amplitude PDF
γ	Exponent of the area and duration relation
V_{av}(t)	Average temporal shape of avalanche
δ	Exponent equal to 2 as predicted by MFT
τ_s	Characteristic time of avalanche decay of the source function
a	Non universal material dependent constant
DSC	Differential Scanning Calorimeter
ϕ_{bl}	Polynomial describe the base line
ϕ_{iex}	Polynomial describe the base line before the peak start

ϕ_{fex}	Polynomial describe the base line after the peak finish
Q	Latent heat detected by the DSC
S_L	Entropy of the transformation detected by DSC
$v(t)$	Velocity of the moving interface at the sensor surface
X	Shift of the moving interface at the sensor surface
L_0	Length of the sample
t_s	Start time
t_f	Finish time
i	Count number
MLE	Maximum likelihood estimator
χ	Exponent of the E and A_m relation
β	Exponent of the S and A_m relation
t_m	Rising time
$\boldsymbol{\rho}$	Asymmetry parameter for number of hits
$\boldsymbol{\eta}$	Asymmetry parameter for Energy
τ_a	Characteristic decay time
$T_p^{DM\rightarrow A}$	DSC peak temperature for the transformation from twinned martensite to austenite
$T_P^{TM\rightarrow A}$	DSC peak temperature for the transformation from detwinned martensite to austenite

Introduction

Shape Memory Alloys, SMAs, form a class of smart materials that can remember their original shape after deforming under an external stimulus, like stress, thermal, magnetic or electric ($\boldsymbol{\sigma}, \boldsymbol{T}, \mathbb{B}, \mathbb{E}$) fields. They have fascinating properties including super-elasticity, super-plasticity, rubber-like behavior, elasto-caloric and magneto-caloric effects. These properties have made them important in many technical applications including medical implants, sensors, robotic muscles, electric and thermal actuators. The physical origin of these behaviors arises from the high crystallographic reversibility between the high symmetry austenite phase, A, and the low symmetry martensite phase, M (observed during martensitic transformation (MT)), or due to the rearrangement of martensite variants like twining ⇆ detwinning.

The structural changes (SCs) in SMAs have jerky character/behavior in which different processes can be involved. These include nucleation, motion of A/M interfaces and/or twin boundaries. These intermittent processes, under slowly changing external driving field, the SCs have stop-and-go activity, and are usually coupled with emission of different avalanches of noise signals (Figure 1). The emitted noise can be acoustic, thermal or magnetic, in case of ferromagnetic SMA.

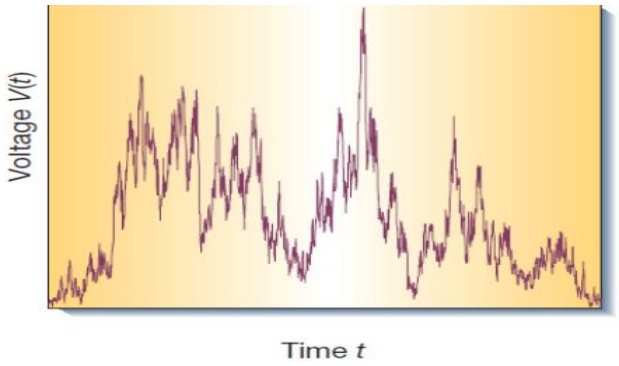

Figure 1 Schematic picture of an avalanche in arbitrary units. Voltage pulse during a single large avalanche (arbitrary units). Notice how the avalanche almost stops several times: if the forcing were slightly smaller, this large avalanche would have broken up into two or three smaller ones. The fact that the forcing is just large enough to keep the avalanche growing is the cause of the self-similarity: on average a partial avalanche of size S will trigger one other of size S [1].

An avalanche can be characterized by its amplitude, A, duration, D, size, $S = \int_0^D V(t)dt$, and energy, $E \propto \int_0^D V(t)^2(t)dt$. Statistically, as it follows from their driven criticality character, each of these parameters follows a damping power law distribution with universal exponents, forming the so-called universality classes [1]. However, these exponents have been proven to be quite robust (i.e. not sensitive enough to the mechanisms) [2]. Recently investigation of different correlation between the AE parameters and the universality of the average temporal shape of avalanches attracted increasing interests [1, 3-4].

The universality is in fact a fingerprint of the similar behaviour of the noises: the temporal shape of a set of such signals looks similar at different time scales over many magnitudes and the averaged shape is the same for a given mechanism (for a given similarity class). Thus, temporal average avalanche shapes (both at fixed duration and area) were studied theoretically and it was proposed that they can be scaled together using two scaling parameters from the above four characteristic quantities [3-4].

At the same time it was also shown that in mean field approximation, MFT, there should exists power relations between *A, D, E* and *S* (for example $E \propto A^3$, or $S \propto A^2$), thus only one scaling parameter would be enough to get scaled temporal shapes [1,3-4]. However, both experiments and theories beyond the MFT suggested that a two –parametrical description should be better. Even, it turned out that there exists an "enigma" [3] for acoustic emission results, since the scaling relations between *E* and *A* as well as between *S* and *A,* rather fulfilled with exponents close to 2 and 1, respectively, instead of 3 and 2. Thus in my theses, during the analysis of experimental data, the above open questions are addressed too.

For my experimental studies $Ni_{49}Fe_{18}Ga_{27}Co_6$ single crystals were selected as a new type of promising ferro-magnetic and high temperature SMAs. These, as compared to the well-studied Ni_2MnGa alloy, are less brittle and by changing the Co content the mechanical and magnetic properties can be finely tuned [5]. These crystals show also a very interesting property: burst like thermal recovery of the shape. While typical MTs take place in about 10-50K wide interval in a DSC curve (taken at the typical 10K/min rate), i.e. the

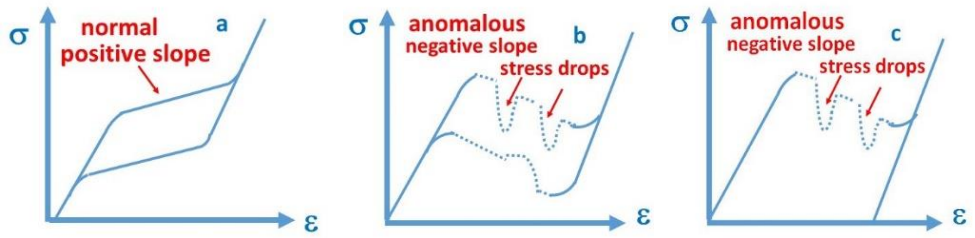

Figure 2 Stress -strain curves at fixed temperature schematically: a) shows a normal super-elastic regime. b) illustrates the anomalous behavior. c) shows the anomalous behavior with a residual strain after which a burst strain recovery can be observed upon heating [7].

duration of the transition is in the order of minutes [6], the burst-like recovery from M → A happens about 2-4 orders of magnitude faster with an audible click. One of the pre-requisites to obtain such burst-like transition is that during uniaxial stress induced $A \rightarrow M$ transformation one should have an anomalous loading stress-strain curve, $(\sigma - \boldsymbol{\varepsilon})$ curve [7].

As it is illustrated in Figure 2 in the normal case (Figure 2a) the stress induced martensite formation takes place along the smooth σ versus ε curve with positive slope (normal superelastic behavior if one also considers the reverse process too). Figure 2b and 2c illustrates the so-called anomalous behaviour: along a certain crystallographic orientation in both cases, the average slope upon loading is negative with local stress-drops on it. Depending on the temperature of the stress induced $A \rightarrow M$ transformation the reverse process, has a jumping character (Figure 2b), or it can happen that below a certain temperature the sample remains in (stabilized) martensitic state after the removal of the stress (Figure 2c). From the latter state, the backward transformation takes place only if one heats up the sample to a temperature higher typically by 30-60 degree than the temperature of the normal thermally induced transformation temperature and with a very narrow temperature interval (burst-like recovery).

Since the understanding of this latter behavior and the explanation of the existence of the stress drops/jumps on the σ versus ε curve were in infancy, I investigated experimentally the details of the above behavior and

the existence of the stress drops by acoustic emission measurements simultaneously with the traditional DSC and stress-strain measurements.

1. Structural changes in shape memory alloys

In this chapter I will present the most important definitions, phenomena and equations proposed in the literature and used in my doctoral research. I will provide these for shape memory alloys (SMA), thermal and stress induced martensitic transformations (MT), acoustic emission (AE) investigations during MT, as well as for self-similar properties of crackling noises.

1.1. Shape memory alloys (SMAs)

As we have seen in the introduction, shape memory alloys are a category of smart active materials that can remember their original shape after deforming under an external stimulus, like stress, thermal, magnetic and electric fields. They are multi-functional materials, which are used in variety of medical and engineering applications including medical implants, sensor, robots, electric and thermal actuators [8-12].

The physical origin of the shape memory behavior in metals is the transformation of the material between two stable crystal structures in a diffusionless manner. This is called martensitic transformation and will be described in detail in the next section.

1.2. Martensitic transformation (MT)

MT takes place by short range, diffusionless, movement of atoms: they move typically less than the inter-atomic distance in the lattice. The process mainly involves two solid phases: traditionally called as austenite, A, as well as martensite, M, phases. The A-phase is a high temperature phase, most frequently, with a cubic structure and can be called as the parent phase. The second phase is the M phase. It is a low temperature phase, with a lower symmetry structure that can be: tetragonal, orthorhombic or monoclinic [12]. The material transforms from A to M on cooling and backwards on heating. An intermittent phase is also possible in some alloys like the R-phase in Cu-based SMAs [13].

During cooling, the MT occurs by formation of differently oriented martensite nuclei (needles) or variants, according to the allowed co-existence of the A and M phases by symmetry relations. These form under the elastic

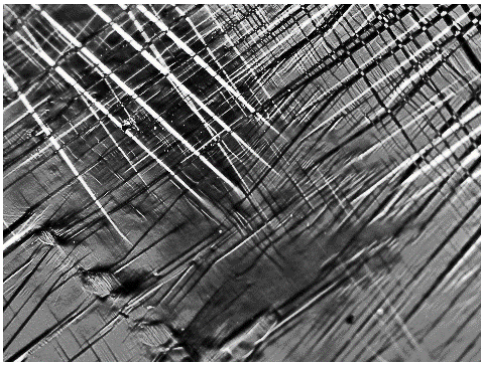

Figure 1.1 Microscopic image of differently oriented needles in $Ni_{49}Fe_{18}Ga_{27}Co_6$ single crystal.

constrain of the austenite: they are arranged to try to keep the original volume/shape of the embedding A-crystal [12].

Figure 1.1, shows a microscopic picture for different martensite variants. If the volume change can be neglected (which is often the case in shape memory alloys) this leads to a shear-like first order phase transformation: the lattice invariant shear can be formed by slips or twinning within the martensite variants. In SMAs the twinning is more favorable (Figure 1.2). If this transformation takes place by cooling, then, due to the formation of differently oriented martensite nuclei, the formed martensite can even contain differently oriented needles, which can be twinned or detwinned: the result is the so called thermally induced martensite, represented in Figure 1.1. Detwinning usually can occur only if the above shape constrain can be resolved (e.g. at an edge of the sample) and the pure shear can be realized: i.e. the twining is a consequence of the shape accommodation in order to decrease the elastic energy, Figure 1.2.

In addition, applying a uniaxial stress on the thermally induced M, it can transform into a stress induced single variant state (which, depending on the stress level can be twinned or detwinned) keeping only that variant which is preferred by the applied stress direction. The structure, obtained after the stress induced variant/twin rearrangement in a thermally induced martensite, is shown schematically in Figure 1.3, where the so called one-way shape memory effect can also be seen.

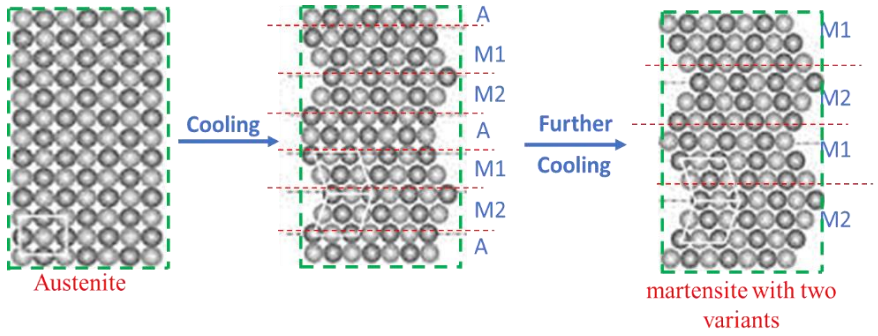

Figure 1.2 Schematic representation of differently orientated martensite twins [14] (twinned martensite) within a certain M nucleus during thermal induced MT; the plane (dashed by red) represents the lattice invariant plane between the two twins. The dashed green lines indicate the shape constrain.

At the same time it can be observed, in the schematic picture shown in Figure 1.3, that if the 2nd step is missing (step b) then a shape change between the 1st and the 3rd structure (a steps to c, directly) can take place during cooling. If by some reason the system "remembers" where such *c*-type martensites have been nucleated, the process can take place backwards (form c to a) on heating: this is the two way shape memory effect (TWSME). It is a synthesized effect i.e. it is possible only after "training" the sample (by cycling during which at a certain place the c-type M can repeatedly nucleate) [8,12].

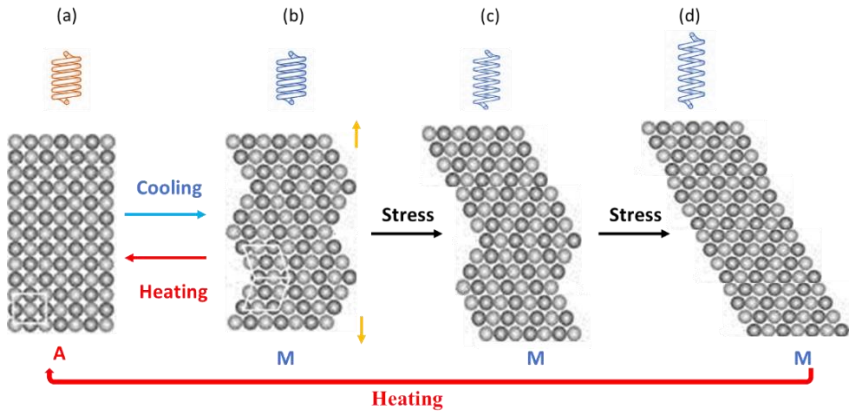

Figure 1.3 Schematic representation of the formation of single variant (detwinned) martensite by the application of uniaxial stress (represented by yellow arrows) after thermally induced M formation. After heating (see the red line on the bottom) the sample turns back to A and recovers the original shape: one-way shape memory effect [14].

1.3. Functional properties of shape memory alloys

As we have seen in the Chapter 1.2, most important applications/properties of SMAs are based on three main effects:

1- The one-way shape memory effect in which the alloy can remember the exact orientation and symmetry of the A-phase, while the M-phase may prefer a different orientation or symmetry [8,12].
2- Thermally induced two-way shape memory effect, as already mentioned, is an acquired effect: the material is able to remember the original shape during thermally induced MT and a reversible shape change is induced. [8,12].
3- Super-elastic and/or rubber-like behaviour: stress induced two-way shape memory effect at constant temperature (see also below).

Figure 1.4 shows summaries of the most important shape memory effect (SME) observed in SMAs due to thermal or stress fields.

The super-elastic behaviour (or pseudoelasticity) [15] starts when the sample is loaded in the A-phase (at point O, in Figure1.4): first the alloy deform elastically and at the martensite start stress, σ_{MS}, a plateau region with small positive slope on the σ versus ε curve (in the two phase A/M region) is formed producing a large recoverable strain (which can be about 10%). When the sample is completely transformed to the M-phase, it continues to deform elastically (at point E) in the formed M-phase. Decreasing the stress (unloading process) the σ versus ε curve has a decreasing part in the two-phase region (from M to A) and the sample recovers to its original shape, with a hysteresis gap.

The superplastic behaviour [9,12,15] can be observed when one applies a stress on the sample below the M_S (M-start temperature), which produces the variant rearrangements (and even detwinning) in the martensite. The loading (AB) part is similar to the superelastic route, athough here there are no phase transformation but rearrangement of M-twins (in Figure 1.4). After removing the stress, the sample remains in the deformed state.

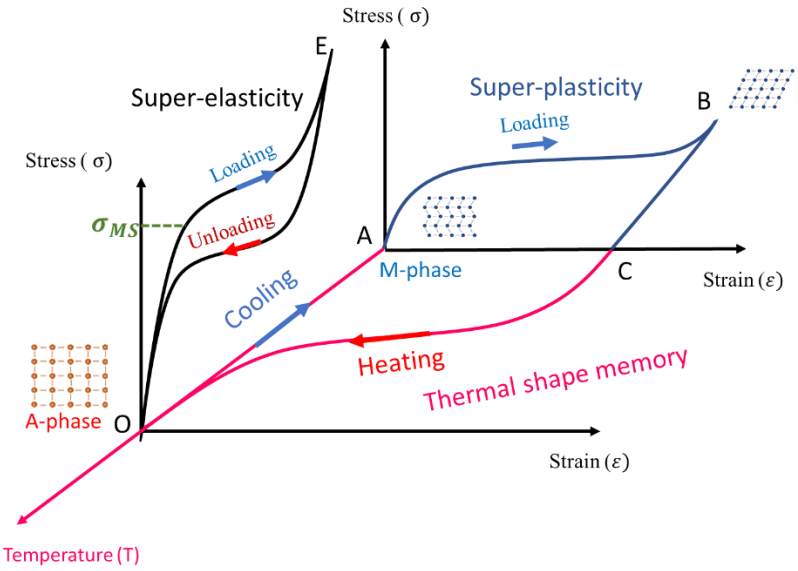

Figure 1.4 Schematic representation for superelasticity, superplacticity and thermal shape memory effect [15].

It can be noted that the application of a special heat treatment (so-called stress induced martensite stabilization, SIM-aging [8]) in the single variant martensitic state under stress, can lead to the so-called rubber like behaviour in the M-state [16-17]. Indeed, it can happen that, re-deforming the M under a stress, the orientation of which is different from that under which the SIM-aging was performed, and then removing the stress, the new (single variant) martensite structure will spontaneously turn back to the stabilized M variant with a detectable shape change (about 4-14%). Thus, this stress induced recoverable (rubber-like) shape change can also be used as a stress induce two-way shape memory function, but sometimes much lower stress is necessary to start the martensite reorientation. Of course, in this case the shape memory is not related to A/M transformation.

Sometimes it was also observed that the transformation had a burst-like character (even the sample had a macroscopic jump) with an audible click. It is documented in the literature that it can take place in forward or reverse/backward transitions or in both [19, 20]. The interpretation of these phenomena is still not fully clear and thus this effect is also the subject of my theses.

1.4. Thermodynamics description of MT

For the thermodynamic description of the MT, if only the temperature and stress can be changed, the Gibbs free energy per unit volume, $g = \frac{G}{V}$, as the function of T, σ and ξ, should be considered. Here $\xi = \frac{v_M}{v_M + v_A}$, is the martensite volume fraction, $v = v_M + v_A$, is the sample volume, T is the temperature, σ is the uniaxial stress. For the A to M transformation (denoted by the $\downarrow$ arrow in upper index) the difference of the g can be written as [18]

$$\Delta g^{\downarrow}(T, \sigma, \xi) = \Delta g^{c\downarrow} + E^{\downarrow} + \mathcal{D}^{\downarrow}. \tag{1.1}$$

Here $E^{\downarrow}$and $\mathcal{D}^{\downarrow}$are the elastic energy and dissipative energy per unit volume, respectively. Δg^{c} is the change in the chemical free energy per unit volume and its ξ dependence can be given as [1.14]

$$\Delta g^{c\downarrow} = \xi g^{M} + (1 - \xi) g^{A} - g^{A} = \xi (g^{M} - g^{A}) \tag{1.2}$$

where

$$g^{M} - g^{A} = \Delta u^{\downarrow} - T\Delta s^{\downarrow} - \sigma \varepsilon^{tr\downarrow}. \tag{1.3}$$

A similar expression holds for the reverse ($M \rightarrow A$) transformation. In Eqn. (1.3) $\Delta u^{\downarrow}$, $\Delta s^{\downarrow}$ as well as $\varepsilon^{tr\downarrow}$ denote the change of the internal energy, entropy and the transformation strain per unit volume in the chemical Gibbs free energy of the M and A phases. These are independent of ξ and they change sign for the reverse transformation ($-\Delta u^{\downarrow} = \Delta u^{\uparrow}$, $\Delta s^{\downarrow} \equiv \Delta s = -\Delta s^{\uparrow}$, and $\varepsilon^{tr\downarrow} = -\varepsilon^{tr\uparrow}$, e.g. $\varepsilon^{tr\downarrow} > 0$ for tension): see also Figure 1.5 for the case when σ=0. The so-called equilibrium transformation temperature is given (taking Eqn. (1.3) equal to zero) by

$$T_o(\sigma = 0) = \frac{\Delta u^{\downarrow}}{\Delta s^{\downarrow}} = \frac{\Delta u^{\uparrow}}{\Delta s^{\uparrow}}. \tag{1.4}$$

Similarly, for T=0, the equilibrium transformation stress is given by:

$$\sigma_o(T = 0) = \frac{\Delta u^{\downarrow}}{\varepsilon^{tr\downarrow}} = \frac{\Delta u^{\uparrow}}{\varepsilon^{tr\uparrow}}. \tag{1.5}$$

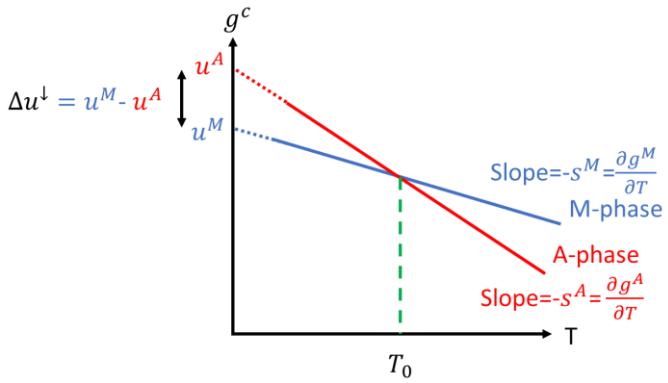

Figure 1.5 g^A and g^M as the function of temperature.

In local equilibrium the derivative of the *total* change of the Gibbs free energy versus the transformed martensite volume fraction, ξ, for the cooling transformation, should be equal to zero [8,10]:

$$\partial(\Delta g^{\downarrow})/\partial\xi = \\ =\partial(\Delta g^{c\downarrow} + E^{\downarrow} + \mathcal{D}^{\downarrow})/\partial\xi = \frac{\partial \Delta g^{c\downarrow}}{\partial\xi} + e^{\downarrow}(\xi) + d^{\downarrow}(\xi) = 0. \qquad (1.6)$$

$e^{\downarrow}(\xi) = \frac{dE^{\downarrow}(\xi)}{d\xi}$ as well as $d^{\downarrow}(\xi) = \frac{d\mathcal{D}^{\downarrow}(\xi)}{d\xi}$, respectively. An expression, similar to Eqn. (1.6), holds for the reverse transformation (with upper index $^{\uparrow}$, taking derivatives by the austenite volume fraction, *1-*ξ). Furthermore,

$$E^{\downarrow}(\xi) = \int_0^{\xi} e^{\downarrow}(\xi)d\xi, \quad \mathcal{D}^{\downarrow}(\xi) = \int_0^{\xi} d^{\downarrow}(\xi)d\xi. \qquad (1.7)$$

The elastic energy is due to the local strain fields around the martensite nuclei formed and to the overlap of their elastic fields: the latter can be proportional to ξ^2 [15] and thus we can assume that;

$$\frac{\partial E^{\downarrow}}{\partial\xi} = e^{\downarrow}(\xi) = e_o^{\downarrow} + \left(e_1^{\downarrow} - e_o^{\downarrow}\right)\xi \quad , \quad \text{with } e_o, e_1 - e_0 > 0. \qquad (1.8)$$

The lower index in $e^{\downarrow}$ indicates the volume fraction of the formed M. Thus $E_e^{\downarrow} > 0$, and for thermoelastic transformations (which are usually observed in SMAs) $E^{\downarrow} = -E^{\uparrow}$ i.e. the same elastic energy is released during heating which was stored during cooling within a cycle (i.e. the integral in Eqn. (1.7) is taken between *0* and *1, for a half cycle*). This also means that [7].

$$\frac{\partial E_e^{\uparrow}}{\partial(1-\xi)} = e_o^{\uparrow} + \left(e_1^{\uparrow} - e_o^{\uparrow}\right)(1-\xi) = -e^{\downarrow}(\xi), \tag{1.9}$$

i.e. we have

$$e_o^{\downarrow} \equiv e_o = -e_o^{\uparrow}, \qquad \text{and} \qquad e_1^{\downarrow} \equiv e_1 = -e_1^{\uparrow}. \tag{1.10}$$

The dissipative energy $\mathcal{D}$ is positive for both directions and can be considered as the sum of two terms $\mathcal{D} = \mathcal{D}_f + \mathcal{D}_n$. The *f* and *n* indexes belong to the classical frictional type dissipation during the motion of the interface between the two phases, while *n* denote the nucleation energy. Since this is always positive in both directions, like the frictional type energy, it can be considered as it would be included in the dissipative term. Thus, we can assume that $\mathcal{D}$ is a monotonic, linearly increasing function of ξ (and it has the same dependence for the reverse transformation as the function of the austenite volume fraction) [7, 18]

$$\frac{\partial \mathcal{D}^{\downarrow}}{\partial \xi} = d^{\downarrow}(\xi) \equiv d_o^{\downarrow} = +d_0^{\uparrow} = d_o. \tag{1.11}$$

This also means that

$$\mathcal{D}^{\downarrow} = \mathcal{D}^{\uparrow}. \tag{1.12}$$

and for a full cycle $\mathcal{D} = \mathcal{D}^{\downarrow} + \mathcal{D}^{\uparrow}$. In addition, using again the notations $\varepsilon^{tr\downarrow}$=-$\varepsilon^{tr\uparrow}$=$\varepsilon^{tr}$ as well as Δs=-$\Delta s^{\downarrow}$=$\Delta s^{\uparrow}$ (Δs<0), the Clausius-Clapeyron equations (taking Eqn. (1.3) equal to zero at fixed, non-zero values of σ and *T,* respectively) are [7,18]

$$T_o(\sigma) = T_o(0) + \sigma\varepsilon^{tr}(\sigma)/-\Delta s\ , \tag{1.13}$$

and

$$\sigma_o(T) = \sigma_o(0)\,\frac{\varepsilon^{tr}(\sigma_0)}{\varepsilon^{tr}(T)} - T\,\frac{\Delta s}{\varepsilon^{tr}(T)} = [T_o(0)-T]\,\frac{\Delta s}{\varepsilon^{tr}(T)}. \tag{1.14}$$

(Regarding the units in Eqns. (1.13) and (1.14) remember that Δs is the entropy change per unit volume, thus e.g. the second term in Eqn. (1.13) indeed has the unit of temperature). Here Eqns. (1.13) and (1.14) were used and it was also taken into account, that the transformation strain, due to the interplay between the formation of the multivariant as well stress induced

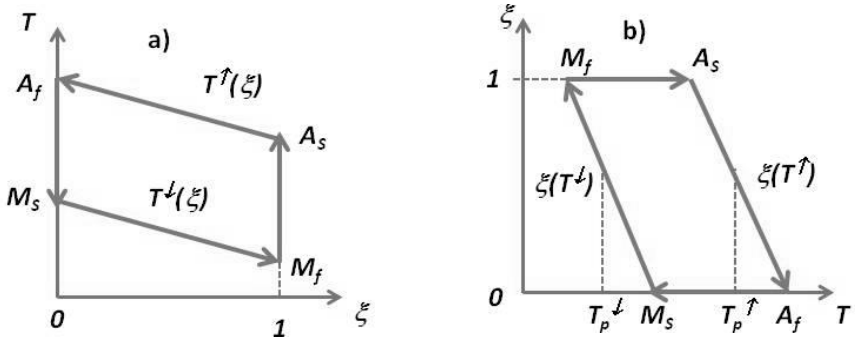

Figure 1.6 Upper and lower branches of the T(ξ) function given by relations (1.15) (a) and its inverse, i.e. the corresponding thermal hysteresis loop (b), schematically. $M_s - M_f$ *and* $A_f - A_s$ *denote the broadening (width) of the transitions (see also the text) [7,18]*

single variant martensite structures (the result of which depends on T and σ) can be temperature and stress dependent [7]: in other words this dependence can be collapsed into a ξ-dependence of ε^{tr} [7, 18, 21]. Eqns.(1.13) and (1.14) give the usually used forms if we assume that ε^{tr} is constant.

General expressions for the down and up branches of the (inverse) thermal hysteresis loop (from Eqns. (1.1)-(1.3) and (1.6)) for $\sigma=0$ (in Eqns. (1.1) and (1.2)) are as follows (Figure 1.6):

$$T^{\downarrow}(\xi) = T_o - \frac{e^{\downarrow}(\xi) + d^{\downarrow}(\xi)}{-\Delta s}, \qquad T^{\uparrow}(\xi) = T_o + \frac{e^{\uparrow}(\xi)+d^{\uparrow}(\xi)}{-\Delta s}, \tag{1.15}$$

(where $e^{\uparrow}(\xi) = \frac{\partial E_e^{\uparrow}}{\partial(1-\xi)}$ and $d^{\uparrow}(\xi) = \frac{\partial \mathcal{D}^{\uparrow}}{\partial(1-\xi)}$). The inverses of these relations are indeed the down and up branches of the thermal hysteresis loops at a fixed value of σ (see Figure 1.6)

Furthermore, the start and finish temperatures are given [7,18] as the limits at $\xi=0$ and at $\xi=1$ in Eqns. (1.15)

$$M_s = T_o - \frac{(d_o^{\downarrow}+e_o^{\downarrow})}{-\Delta s}, \qquad M_f = T_o - \frac{(d_1^{\downarrow}+e_1^{\downarrow})}{-\Delta s},$$
$$A_f = T_o + \frac{(d_o^{\uparrow}+e_o^{\uparrow})}{-\Delta s}, \qquad A_s = T_o + \frac{(d_1^{\uparrow}+e_1^{\uparrow})}{-\Delta s}. \tag{1.16a}$$

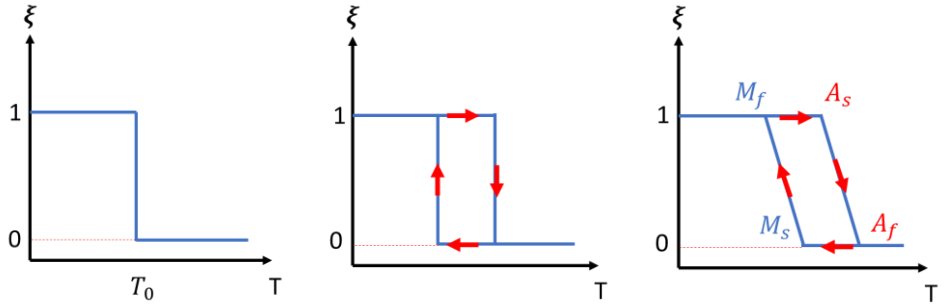

(a) (b) (c)

Figure 1.7 Simplified schematic representation of hysteresis loop [2]. The start and finish temperatures are also indicated (see also the text): a) $e(\xi) = d(\xi) = 0$*, the forward and reverse transformation take place at* T_0*, b)* $e(\xi) = 0, d(\xi) = constant$*, the forward and reverse transformation take place at different temperatures, the hysteresis loop is already manifested.*$d(\xi) = constant$*, and* $e(\xi)$ *linearly depends on* ξ*, the hysteresis curve is tilted.*

which, using the simplifying assumptions in Eqns. (1.10) and (1.11), can be rewritten as:

$$M_s = T_o - \frac{(d_o+e_o)}{-\Delta s}, \quad M_f = T_o - \frac{(d_o+e_1)}{-\Delta s},$$
$$A_f = T_o + \frac{(d_o-e_o)}{-\Delta s}, \quad A_s = T_o + \frac{(d_o-e_1)}{-\Delta s}. \tag{1.16b}$$

According the results obtained above, the main (schematic) features of the thermal hysteresis loops can be summarized (using also the simple limits as introduced above) as illustrated in Figure 1.7. It can be seen that T_o would be directly obtained only if both the first derivatives of the elastic and dissipative energies would be zero (Figure 1.7a). If the first derivative of the elastic energy is zero, but d_o is constant (Figure 1.7b) a hysteresis is observed and the area of the loop is given by (see Eqn. (16b)).

$$A_s - M_s = \frac{2d_0}{-\Delta s}, \tag{1.17}$$

i.e.

$$\mathcal{D} = \mathcal{D}^{\downarrow} + \mathcal{D}^{\uparrow} = 2d_o = -\Delta s(A_s - M_s). \tag{1.18}$$

In case of c) in Figure 1.7 the slopes of the down and up branches are given as

$$M_s - M_f = -\frac{e_1 - e_o}{-\Delta s} \quad \text{and} \quad A_f - A_s = \frac{e_1 - e_o}{-\Delta s}, \tag{1.19}$$

respectively, i.e. the inclinations of the corresponding branches of the thermal hysteresis loop are the measures of the slopes of the first derivatives of the elastic energy (see also Eqn. (1.8)).

Eqn.(1.15) (see also Figure 17.c) expresses that e.g. during cooling at a certain temperature the state is in equilibrium at a fixed ξ. If the cooling would be stopped no further change could happen. In order to proceed one has to decrease the temperature (the change of the chemical energy is proportional to ΔT: see also the inverse of Eqn. 1.15): after the transformation of some additional M the change in the elastic energy will compensate the change of the chemical energy cause by ΔT; this is the so called the thermoelastic equilibrium.

Similarly as Eqns. (1.15) were obtained from Eqns. (1.1)-(1.3) and (1.6) we can get, (for constant ε^{tr}) the schematic σ versus ξ functions at *T=const.* as

$$\begin{aligned} \sigma^{\downarrow}(T, \xi) &= \sigma_o(T) + \frac{e^{\downarrow}(\xi) + d^{\downarrow}(\xi)}{\varepsilon^{tr}}, \\ \sigma^{\uparrow}(T, \xi) &= \sigma_o(T) + \frac{e^{\uparrow}(\xi) + d^{\uparrow}(\xi)}{\varepsilon^{tr}}, \end{aligned} \tag{1.20}$$

and $\sigma_o(T)$ is given by Eqn. (1.14). The start and finish stresses (similarly as Eqn. (1.16a) were obtained as the limits at *ξ=0* and at *ξ=1* of Eqn. (1.20) and using the simplifying assumptions in Eqns. (1.10) and (1.11), for both the forward and reverse transformations), can be given (for constant ε^{tr} [7]) from Eqn. (1.20) as

$$\begin{aligned} \sigma_{M_s}(T) &= \sigma_o(T) + \frac{e_o + d_o}{\varepsilon^{tr}} \\ \sigma_{M_f}(T) &= \sigma_o(T) + \frac{e_1 + d_0}{\varepsilon^{tr}} \\ \sigma_{A_s}(T) &= \sigma_o(T) - \frac{-e_1 + d_0}{\varepsilon^{tr}} \\ \sigma_{A_f}(T) &= \sigma_o(T) - \frac{-e_o + d_o}{\varepsilon^{tr}}. \end{aligned} \tag{1.21}$$

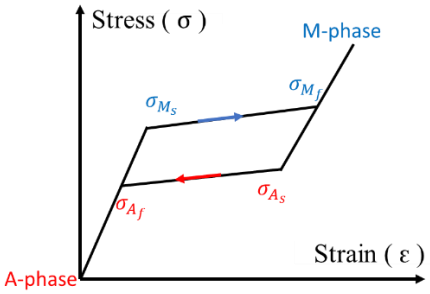

Figure 1.8 Schematic representation for the σ versus ε hysteresis loops

It has to be noted the d_o, e_o and e_1 can be different for a thermal hysteresis loops than here: the development of the martensite microstructure can be quite different for the growth of a multivariant or single variant martensite. The above results can be compared to the experimentally observed σ versus ε hysteresis loops (Figure 1.8), if we assume that in the part belonging to the phase transformation the strain is proportional to ξ ($\varepsilon \propto \xi$). The first and last linear parts correspond to the elastic deformation of the austenite and martensite (i.e. according to the Hook-law the slope of these parts gives the stiffness of the A and M phases ($\boldsymbol{S}_A$ and $\boldsymbol{S}_M$, respectively). Furthermore, the slopes of the up- and down-branches are proportional to:

$$\sigma_{M_f} - \sigma_{M_s} = \frac{e_1 - e_o}{\varepsilon^{tr}} \quad \text{and} \quad \sigma_{A_f} - \sigma_{A_s} = -\frac{e_1 - e_o}{\varepsilon^{tr}}, \tag{1.22}$$

i.e. the slopes of the transition regions are the measure of the first derivative of the elastic energy. Furthermore, the area of the hysteresis loop is given approximately by

$$\mathcal{D} = \left(\frac{\sigma_{M_s} + \sigma_{M_f}}{2} - \frac{\sigma_{A_s} + \sigma_{A_f}}{2}\right) \varepsilon^{tr} = 2d_o. \tag{1.23}$$

Closing this section, it is worth emphasizing that although the above simplified description gives almost all most important characteristics of martensitic transformation in shape memory alloys, in real experimental situations quite a large variety of violations of some of the above assumptions can be found. Such examples can be the so-called asymmetry of the transformation when the up- and down-branches can have different slopes (see e.g. [22]), or the so-called anomalous stress-strain loops, when the slope of the up-branch can be negative and even stress drops can be observed on it [7] (see also below in the discussion chapter of my experimental results).

1.5. On the jerky character of structural changes in SMAs

A quite large number of phenomena are known to produce crackling noises (noise avalanches) which can be defined as series of discrete events snapping broad range of sizes. This includes earthquakes, sand-piles, plastic deformation, Barkhausen noise, etc... The structural changes during MT under an applied external field also proceed with discontinuous motion of the A/M interfaces which can produce crackling noise. The most important general feature of crackling noises [23] is that they show similar statistics, which is a consequence of their self-similar behaviour. The avalanches are jerky responses to slowly changing driving force or field and are fingerprints of the so-called driven (tuned) criticality [23], resulting in a truncated power-law behavior [24,25]. The probability density of a given quantity, x (e.g. amplitude, A, energy, *E,* size, *S,* or duration time, *D,* of individual noise signals), can be given as

$$P(x) = cx^{\mu} exp\left(-\frac{x}{x_c}\right) \tag{1.24}$$

where c is the normalization constant, μ is the characteristic exponent, and x_c is the cutoff value. Thus, *A* corresponds to the V_{max} (see Figure. 1 in the chapter of general introduction) *D* is the whole duration, and *S* and *E* are defined as follows [1]

$$S = \int_0^D V(t)dt \tag{1.25}$$

$$E = \frac{1}{R}\int_0^D V^2(t)dt, \tag{1.26}$$

where *R* has unit of Ohm (remember for the classical expression in the electrodynamics for the power, P; $P = \frac{V^2}{R}$) and is constant in given material.

The power-law distributions reflect the self-similar behavior: the temporal shape of a set of such signals looks similar at different time scales (Figure 1.9) Indeed self-similar signals can be described mathematically by a power law: $(x) = x^{\mu}$, $f(\lambda x) = \lambda^{\mu} x^{\mu}$. The theory of such processes is quite

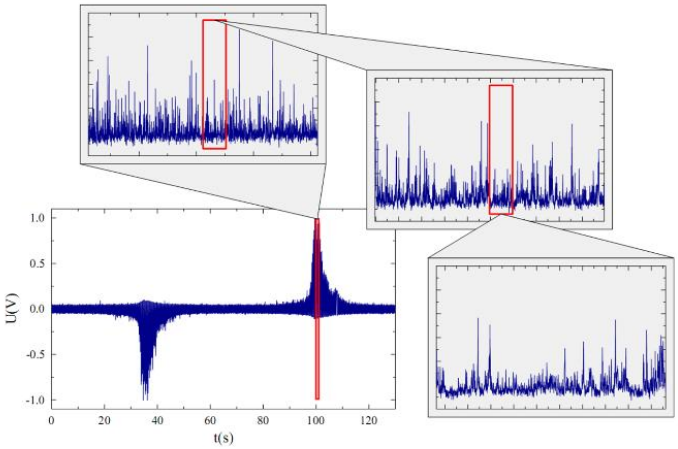

Figure 1.9 Voltage signals from Barkhausen noise at different time scales [27]

sophisticated [1, 28] and based on the co-called interface depinning models and use the renormalization group theory.

However, based on the above self-similarity, it is relatively easy to derive power law relations between the measurable parameters (*A, E, S, D)* or between the characteristic exponents of the above parameters. Let us see this on the example of the relation between *S* and *D.* We have just to compare the averaged and scaled *S(D)* function to itself by expanding the time scale by a small factor [29] as follows. Rescale both the *S* and *D* by appropriate scaling factor, S_s and D_s, respectively.

$$S(D) = S_s f\left(\frac{D}{D_s}\right). \tag{1.27}$$

As a next step expand the time scale by a small factor $D_s = \frac{1}{1-\delta}$. Then rescaling of the size will also be small: $1+\gamma\delta$, i.e.

$$S(D) = (1+\gamma\delta)S\big((1-\delta)D\big), \tag{1.28}$$

which, for very small value of δ, has the form

$$\gamma S = D\frac{\Delta S}{\Delta D} \cong D\frac{dS}{dD}, \tag{1.29}$$

where it was used that $\Delta D = D - D(1-\delta) = \delta D$, and $\Delta S = S$ Now, the solution of Eqn. (1.29) has the form

$$S \propto D^{\gamma}. \tag{1.30}$$

Using similar considerations, relations between the other parameters can be obtained [24, 27-30] as:

$$A \propto D^{\gamma-1}, \tag{1.31}$$

$$E \propto A^{\frac{2\gamma-1}{\gamma-1}}, \tag{1.32}$$

$$S \propto A^{\frac{\gamma}{\gamma-1}}. \tag{1.33}$$

Similarly, it can be shown [1, 30-32] that the following relations exist between the exponents

$$\frac{\boldsymbol{\tau}-1}{\boldsymbol{\varepsilon}-1} = 2 - \frac{1}{\gamma}, \tag{1.34}$$

$$\frac{\boldsymbol{\alpha}-1}{\boldsymbol{\varepsilon}-1} = \frac{2\gamma-1}{\gamma-1}, \tag{1.35}$$

where τ, ε and α denote in Eqn. (1.24) the characteristic exponents for the area, energy and amplitude, respectively.

Furthermore, using again the self-similarity [1], it can be shown that the average temporal shape of an avalanches at fixed duration should have the form

$$V_{av}(t, D) = D^{\gamma-1} V(\frac{t}{D}) \tag{1.36}$$

where $V\left(\frac{t}{D}\right)$ is universal function of $\frac{t}{D}$, t donates the time. It can be seen from the above results that the parameter γ plays a central role if one wants to compare the experimental results with the predictions of the theory. The theoretical models (e.g. based on the interface depinning model in the framework of the renormalization group theory, as it was mentioned above) provide values for γ between 2.0 and 1.5. In fact these two values correspond to the so-called long-range elastic interaction limit (or the limit of the mean field theory, MFT) [33] as well as to the short-range elastic interaction limit, respectively, between the moving interface and the pinning points). Thus, crackling noise systems can be grouped into universality classes on the basis of the observed γ, or on the basis of the obtained power exponents as given by Eqns. (1.30) -(1.33). Note, that since the differences of the exponents between

the above two mechanisms are rather small (the typical error for the experimental exponents is ±0.05-0.1) it is not easy to make a clear distinction between the different mechanisms on the basis of the exponents alone. In other words: the power laws are quite robust, the self-similarity itself dominates and the power exponents do not differ considerably for different mechanisms. This is why it became a trend in the last decade to go beyond the power laws [28, 34 - 36] and investigate the temporal shapes of avalanches even beyond the MFT. Thus, it was obtained that the temporal shape of avalanches can be given by:

$$V_{av}\left(\frac{t}{D}\right)D^{1-\gamma} = \left[\frac{t}{D}\left(1-\frac{t}{D}\right]^{\gamma-1}\left[1-A(\frac{t}{D}-\frac{1}{2})\right], \tag{1.37}$$

and

$$V_{av}(t) = atexp(-\left(\frac{t}{\tau_s}\right)^{\delta}) \tag{1.38}$$

for fixed duration time and area, respectively. In Eqn. (1.37) A is the skewness parameter (asymmetry factor) and can be different for different universality classes (i.e. for different γ). In Eqn. (1.38) a and τ_s are are non-universal (material-dependent) constants and $\delta = 2$ in MFT.

Although, the fact that, self-similarity of crackling noises implies scaling relations between avalanche parameters were $E \sim A^{\frac{2\gamma-1}{\gamma-1}}$ and $S \sim A^{\frac{\gamma}{\gamma-1}}$. According to the theoretical prediction given by the main field theory, MFT, this should give back the γ = 2. However, the exponents obtained from AE experiments contradict to the above theoretical predictions leading to the so-called enigma. It will be a part of my thesis to analyse the details of this problem.

2. Experimental and evaluation techniques

AE spectroscopy is an important tool for characterizing structural changes in SMAs. In our research team, it is possible to utilize the AE measurements simultaneously with thermal and mechanical tests. The investigated sample, $Ni_{49}Fe_{18}Ga_{27}Co_6$ (at%) single crystal, was provided by our cooperating partner, Tomsk State University, Russia. In this chapter, an overview of the used samples, the experimental setups (DSC, tensile machine, detection of AE signals), and the method for the evaluation of critical exponents will be provided.

2.1. The sample

The $Ni_{49}Fe_{18}Ga_{27}Co_6$ (at%) alloy was prepared using vacuum induction melting. The single crystals were grown by Bridgman method in helium atmosphere at Tomsk State University, Russia. The as-grown crystals were annealed at 1473 K for 1h in argon atmosphere at a temperature well above the order-disorder transition temperature ($T \cong 975\ K$ [37, 38]), and then water quenched. The B_2 (disordered) high temperature phase of the quenched crystals undergoes a martensitic transformation to the $L1_0$-martensite. According to the results of TEM investigations [37, 38] the above homogenization and quenching resulted, immediately after quenching, in the presence of γ-phase precipitates with a size of 5-15 μm [5, 37, 39]. Also, see Figure 2.1.

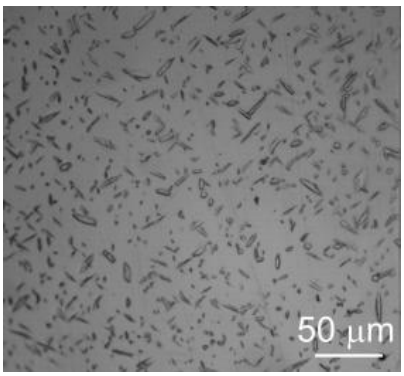

Figure 2.1 Optical micrograph from $Ni_{49}Fe_{18}Ga_{27}Co_6$ single crystals annealed at 1473K and quenched in water with formed γ-phase particles [39].

Sample A was cut with dimensions 1mm×1.5mm×2mm and mass 16mg from the as grown piece and then heat treated as mentioned above. This sample was kept for 3-months at room temperature after quenching, before carrying the measurements. The small dimensions and low mass of the sample make it suitable for investigation of stress-strain curve and the burst strain recovery in the DSC, in which jumping of the sample with an audible click is involved.

Sample B was cut as a disk shape sample with diameter 3mm, thickness 0.2 mm and mass 16mg from as grown piece then heat treated as mentioned above. The disk shape sample provided a good thermal contact with the DSC pan and make it perfect for thermal and acoustic emission investigation.

Sample C was cut for two pieces after the above heat treatment: Piece 1 with dimension 1.9mm×2.2mm×1.3mm and mass 49 mg which is good for the DSC investigations. Piece 2 with dimension 1.9mm×2.2mm×3.0mm and mass 104 mg was used for the simultaneous measurements of the stress-strain curves and AE.

The cutting of the samples was performed using a spark erosion machine. Table 2.1 provides a summary of information regarding these samples [6].

Table 2.1 Samples description.

Sample	Shape	Size	Mass	Heat treatments
A	rectangular	1 mm×1.5 mm×2 mm (Stress-strain + DSC)	16 mg	1h at 1473 K in argon atm., quenched + kept at room temperature for 3 months
B	Disk	diameter: 3 mm thickness: 0.2 mm (DSC)	16 mg	1h at 1473 K in argon atm., quenched
C	Rectangular	1.9mm×2.2mm×1.3mm (DSC) 1.9mm×2.2mm×3.0mm (Stress-strain)	49mg 104 mg	1h at 1473 K in argon atm., quenched

2.2. Experiment 1: DSC, peak analysis and acoustic emission (AE) measurements

For my measurements, I used **PerkinElmer's power compensation DSC7**, Figure 2.2, with scanning rate 10 K/min.

The DSC calibration was based on the heat of fusion of pure indium and the melting points of pure indium and zinc, both calibration samples have well defined melting peak and good thermal conductivity. In some measurements, the DSC was cooled down to -40 ^{o}C by freezing the refrigerant with liquid nitrogen, LN2, because for some samples the transformation temperature was low. In the latter case, I made calibration after adding the liquid nitrogen in order to ensure the precise control and baseline stability of the DSC. In addition, to prevent oxidation at high temperatures, flowing nitrogen gas (N_2) was used.

For the **DSC peak extraction** I determined the start and finish temperatures using the cross-cut/first derivative methods both gave the same result within the error bars. For the baseline removal; it was evaluated by numerical method through fitting polynomials for the baselines before, ϕ_{iex}, and after, ϕ_{fex}, the transition peak. I calculated the baseline during the transition by weighting the above polynomials by the transformed fraction, α, $\phi_{bl} = (1-\alpha)\phi_{iex} + \alpha\,\phi_{fex}$. Fortunately, for my case $\phi_{iex} \cong \phi_{fex}$ [40].

Figure 2.2 PerkinElmer's DSC 7

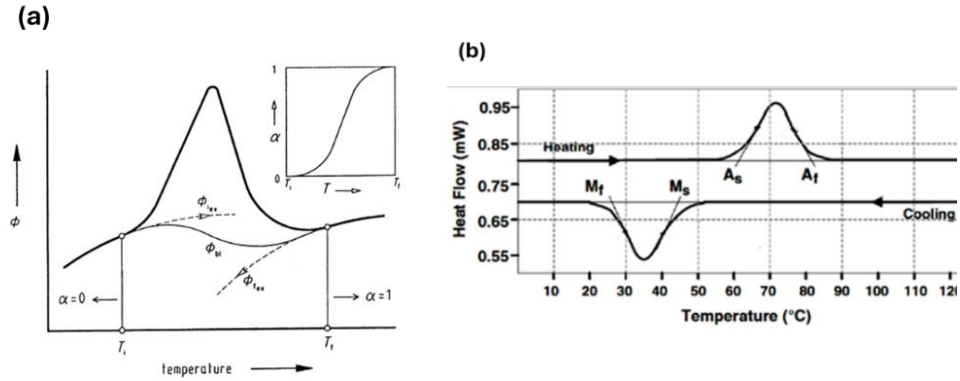

Figure 2.3 labeled schematic representation for the DSC -peak [40] (a)*, DSC peaks for heating and cooling after baseline removal [11] (b).*

Figure 2.3b, shows a schematic representation for the heating/cooling peaks ready for evaluation. The transformation from A → M usually involves heat releaseing (exothermic transition), while the backward transition M → A is accompanied with heat absorption (endothermic transition).

Once I extracted the peak, I could calculate the different thermal parameters. Since the heating/cooling rate, (dT/dt), was kept constant during the measurement, the heat of transformation (Q) could be calculated from the area under the peak as follows:

$$Q = \int_{t_s}^{t_f} P dt = \frac{1}{dT/dt} \int_{T_s}^{T_f} P \, dT \qquad (2.1)$$

Where P is the subtracted/added power required to keep a constant heating/cooling rate and t represents the time. The lower index s and f indicate the start and finish points.

The entropy (S_L) can be calculated from the following integration, as:

$$S_L = \int_{T_s}^{T_f} \frac{dQ^{\downarrow}}{T}, \qquad (2.2)$$

using that the specific heat per unit mass is defined as $c_p = \frac{dQ}{dT}$, i.e. $dQ = c_p dT$. Eqns (2.1) & (2.2) are obtained under the assumption the C_p is approximately the same for the A and M phases.

The volume fraction of martensite as a function of temperature can be obtained as [21,41]:

$$\xi\left(T^{\downarrow}\right) = \int_{M_s}^{T} \frac{dQ^{\downarrow}}{T} / \int_{M_s}^{M_f} \frac{dQ^{\downarrow}}{T} \tag{2.3}$$

$$\xi\left(T^{\uparrow}\right) = \int_{A_s}^{T} \frac{dQ^{\uparrow}}{T} / \int_{A_s}^{A_f} \frac{dQ^{\uparrow}}{T} \tag{2.4}$$

Both Eqns. (2.3) & (2.4) are used to construct the up and down branches of the thermal hysteresis loop [21] (see the next chapter).

The simultaneous DSC & AE measurements were made using a homemade accessory. The microphone was coupled to a steel waveguide, of 15mm length, in order to provide thermal isolation from the sample when its temperature was widely varied. The microphone and the waveguide were coupled by grease to improve the acoustic signal transfer. For the hit mode, the threshold level was determined from measurements carried out in austenitic state for cooling and martensitic state for heating, respectively (see Figure 2.4).

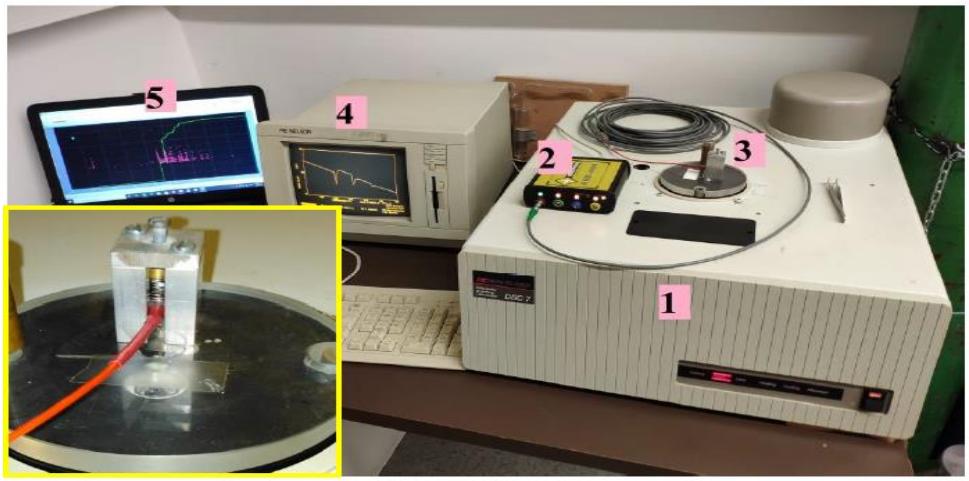

Figure 2.4. Schematic representation for the setup use in the simultaneous DSC and AE measurement. (1) DSC, (2) Sensophone, (3) microphone+ wave-guide housing, see the enlarged image. (4) DSC controller and (5) AE control computer [42].

2.3. Experiment 2: tensile machine and AE measurements

Instron testing machine 4465 was modified for dynamic high precision strain controlled experiments. The machine was adapted with two steel anvils, fixed lower anvil and dynamic upper anvil, for compression of small samples in mm-scale. A load cell was also connected to the upper anviel with a force capacity 1000±10 N. Two Arduino UNO micro-controllers works as interface between the machine and computer. The first controller maintains a constant strain rate by controlling the motor based on feedback from the encoder, which tracks the position of the upper anvil. The second controller collects the data from the load cell in real time. The data acquisition rate, the frequency at which the datapoints are collected over time, was 1000 Hz.

I made compression dynamic measurements with a constant strain rate $0.003s^{-1}$ and $0.0017s^{-1}$ for samples A and C, respectively. The temperature was controlled by a proportional-integral-derivative controller (UNICOUNT, PMG-400, Universal controller and display unit) which provides a constant temperature with ± 5 ℃ accuracy. The temperature was measured by a copper-constantine thermocouple fixed with Teflon tape, into the lower anvil quite close to the sample (see the insert in Figure 2.5). For high temperature measurements, the sample was heated by 2- halogen lamps fixed to aluminium heating chamber. For low temperature measurements, the cooling was controlled by pumping liquid nitrogen into the cavity of the aluminium chamber. The load cell was protected from the different temperature by aluminium sheets acting as heat retarders/dissipaters. The samples A and C have a rectangular shape so placing them in our arrangement was quite easy, see Figure 2.5.

For the **simultaneous measurement of AE during compression test**; the AE sensor (microphone) was fixed to the top steel pushing head. This was because of the small dimension of the sample and to provide an isolation for the microphone at different temperatures. Grease was applied between the microphone and the steel pushing head. For the hit mode, the threshold level was determined from measurements carried out when the upper anvil is connected to the sample with force 1-5N, at each temperature, see Figure 2.5.

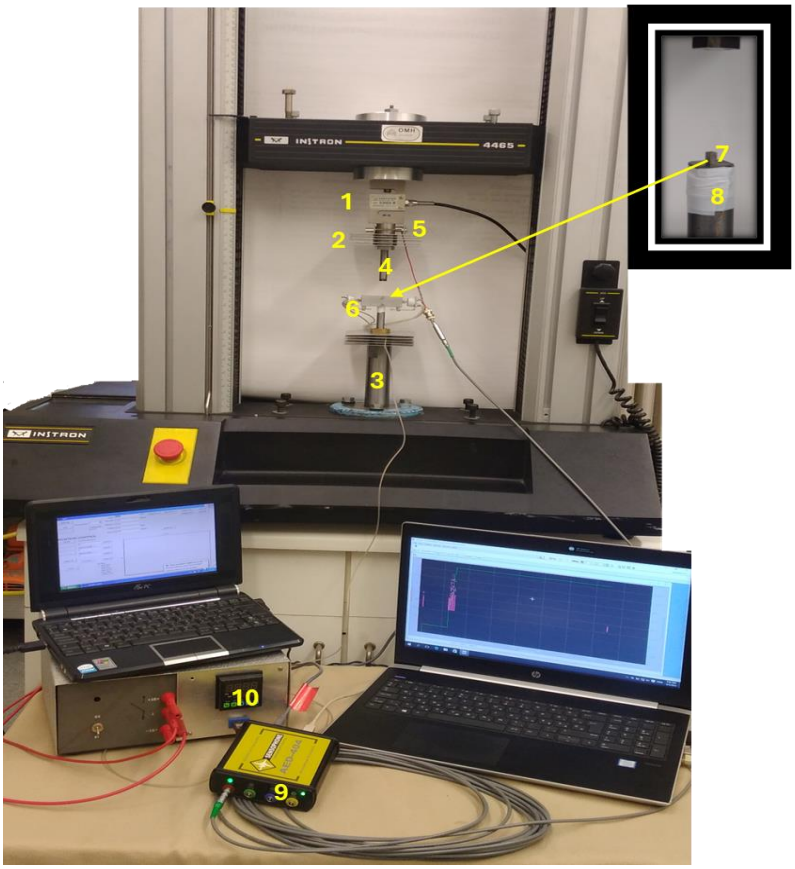

Figure 2.5 (1) Force sensor, (2) Heat retarder made of aluminium sheets, (3) Lower anvial fixed, (4) Upper anvil dynamic, (5) Piezo-electric microphone, (6) Halogen lamp Furnace, (7) The sample, (8) Thermocouple fixed by teflon tape, (9)Sensophone, (10)Temperature controller.

Usually, I heated/cooled the sample to the required measuring temperature waited 5-10 min for the homogenization/stabilization of the temperature and started the measurements.

2.4. AE sensor and data acquisition unit

The following **piezoelectric microphone** was used: MICRO-100s from Physical Acoustic Corporation, Princeton junction, USA. It has a good frequency response between 100 KHz and 1 MHz, which is nearly flat in the range 0.2 – 1MHz, (at about ~75 dB in average) with maximum ± 10dB deviation (1V reference value). The microphone was integrated with a 30 dB pre-amplifier. Furthermore, we connected a primary amplifier to the

microphone with logarithmic gain, offering a dynamic range of 90 dB and operating within a band pass frequency range of 30 KHz to 1 MHz.

The AE sensor was connected to **Sensophone AED404** Acoustic Emission Diagnostic Equipment (Geréb and Co.,Ltd.,Budapest, Hungary). It controls the signal, preforms the data acquisition and analyses the AE signal.

Two methods of data acquisition were used;

i) Streaming mode: continuous acquisition of raw signals with a maximum 8MS/sec sampling rate.

ii) Hit mode: the device processes the signal in real time, and it stores only the avalanche parameters (amplitude, duration, counts, rise time, etc), this included removing signals below the threshold. The sampling rate was 16MHz.

2.5. Evaluation of AE signals.

It was mentioned in the previous chapters that the intermittent motion of A/M interfaces results in emission of elastic waves, which travel through the material and the transducer. The source signal (which is the local strain change during a "jump" of the interface) creates characteristic ringing, at the self-frequency of the detection system, and after propagation and attenuation reaches the surface of the detector. This causes a recorded voltage signal (V(t)), which is proportional to the displacement rate (the velocity) of the moving interface $v(t)$ at the surface of the sensor.

$$V(t) \sim v(t) \sim \frac{dX}{dt} \sim L_0 \frac{d\varepsilon}{dt} \tag{2.5}$$

X, ε represent the shift in the interface at the sensor and the corresponding strain, respectively. L_0 is the length of the sample. Figure 2.6 shows a schematic picture of the detected voltage in AE measurement in a real experiment: the attenuation and ringing are well visible.

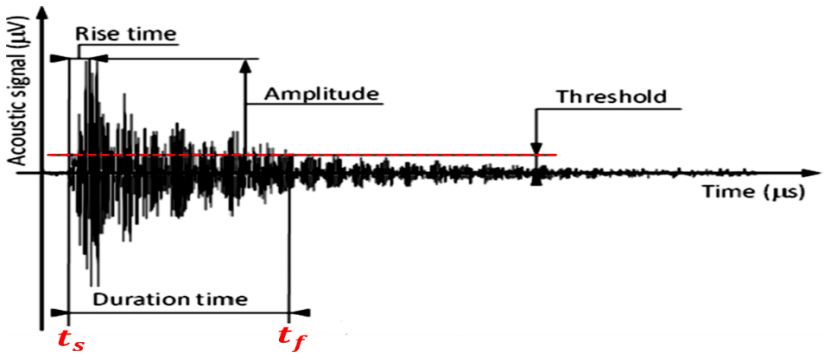

Figure 2.6 Temporal shape of acoustic emission signal (many signals, sub-avalanches, following each other within one avalanche and echoes of the wave from the sides of the sample), the duration, $D = t_f - t_s$, (t_s and t_f are the start and finish times for an avalanche, where the signal goes above and below the threshold value, respectively.) amplitude, A, is, by definition, the maximum voltage within an avalanche, the rise time, t_m, is the time needed from t_s to reach the maximum voltage [43].

In accordance with Figure 2.6, from the collected row signals one can determine the amplitude, *A,* the duration time, *D*, as well as calculate the energy, E, and area, S, of avalanches as:

$$E = \int_0^D \frac{V(t)^2}{R} dt \qquad (2.6)$$

where R is an arbitrarily chosen resistance (I used R=1Ω), and

$$S=\int_0^D V(t)dt. \qquad (2.7)$$

The problem whether the detected signal, V(t), correctly reflects all the characteristic features of the source signal or not, is a delicate question in the literature [3] and called as the transfer problem for AE measurements.

It is already clear from Figure 2.6 that while the maximum amplitude, A , and rising time can be well proportional to the source signal, the duration time can be well distorted since the exponential attenuation of the elastic waves can considerably distort this value: see Figure 2.7. In addition, the values of E and S, as calculated from the integration over the duration time, can also be distorted, especially for shorter duration of the source signal, resulting in the so-called enigma in the scaling relation of the AE, as described below.

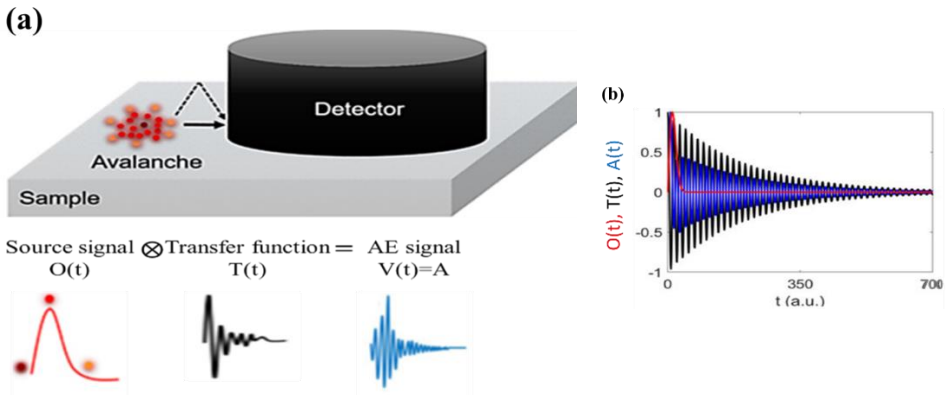

Figure 2.7 Schematic representation for the distortion of the source signal(a) The distortion is manifested in the time scale, in which the transfer function resulted in a long exponential decay tail at the end of the avalanche, reflected in the duration of the avalanche, while the amplitude and rising time are not/less distorted(b)[3].

Self-similarity of crackling noises implies scaling relations between avalanche parameters were $E \propto A^{\frac{2\gamma-1}{\gamma-1}}$ and $S \propto A^{\frac{\gamma}{\gamma-1}}$ [1, 3, 4]. According to the theoretical prediction given by the main field theory, MFT, this should give back the $\gamma = 2$ (see: Chapter 1.5 and Eqns. 1.31-1.33). However, the exponents obtained from AE experiments contradict the above theoretical predictions leading to the so-called enigma [3]. Thus, it was proposed [3] that the reason of the enigma is the fact that the detected AE emission signals are distorted, and this causes deviations from the theoretical predictions. For instance it results in elongation of the tail of avalanche, increasing the avalanche duration time, D. It will be a part of my thesis to analyze the details of the above problem (see next Chapter 3.1.3).

The exponents of the probability distributions of the evaluated parameters (see also Eqn. (1.24) in Chapter 1.5) was calculated using two methods: directly plotting the log P(x) versus x, as well as by the application of the maximum likelihood estimation.

The probability density of a given quantity is evaluated by creating a histogram on log-log plot with a constant logarithmic width, $b = \log(x_{i+1}) - \log(x_i)$. The counts are then divided by the sum of all the counts and normalized by the linear width of the bin, $b = x_{i+1} - x_i$; this is the case of logarithmic pinning [44]. The exponent (μ) are then estimated by using a two

parametric nonlinear fitting using Levenberg-Marquadt least square method using Eqn. (2.6).

$$P(x) = cx^{\mu} \tag{2.6}$$

Where c is the normalization constant. Regarding the cutoff factor in Eqn.(1.24) either $exp\left(-\frac{x}{x_c}\right) \cong 1$ was assumed (when the x_c was not visually recognized) or I made fit only in the linear regime as it is illustrated in Figure 2.8a. On the other hand, the maximum likelihood estimator (MLE) was used to estimate μ, using Eqn. (2.7), in which the relation between μ and x_{min} was obtained by maximizing the likelihood function [43, 45] (see Figure 2.8b). x_{min} is the smallest data for which the calculation was preformed.

$$\mu = 1 + n[\sum_{i=1}^{n} ln\frac{x_i}{x_{min}}]^{-1} \tag{2.7}$$

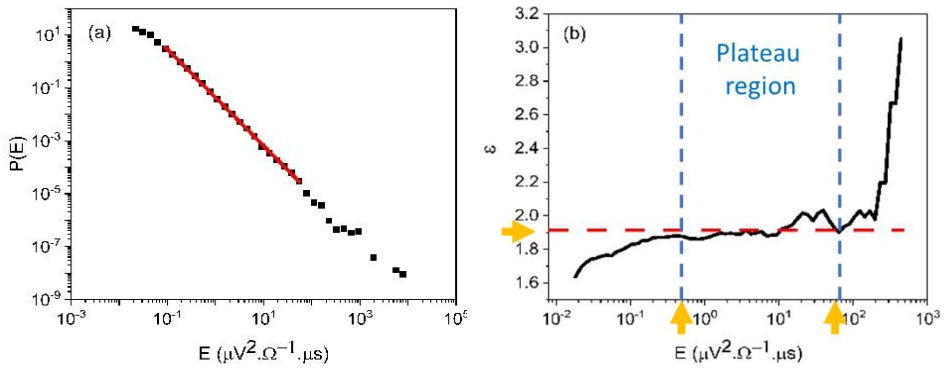

Figure 2.8 Probability density function, PDF, of energy, the x_c is evaluated visually at the point where the line deviates from the linear behavior(a) and corresponding maximum likelihood, ML, representation, the plateau region represent the range in which the exponent become independent of lower/upper cutoff, between the dashed lines. The true values for energy exponent,ε, is marked by yellow arrow on the vertical, on the figure(b).

3. Results and discussion

In the first part of this chapter the DSC results for thermally induced MT as well as the results of AE, simultaneously measured with the DSC, are provided. The experimental and theoretical investigations of the scaling relations E~A^{χ}, S~A^{β} and the average shape of avalanches are also presented and discussed. In the second part, the burst like transition as well as the results of AE, simultaneously measured with the DSC, are provided. Results of the anomalous stress-strain curves for superelastic regime, measured simultaneously with AE, are also presented. The discussion proposes explanations and provides comparison between thermal and stress induced MTs. The above results were published in my papers [4, 7, 6].

3.1. DSC and AE results for thermally induced MT

In Figure 3.1 I show the **DSC results** for heating and cooling of samples (measured with 10K/min scanning rate) A, B and C, respectively.

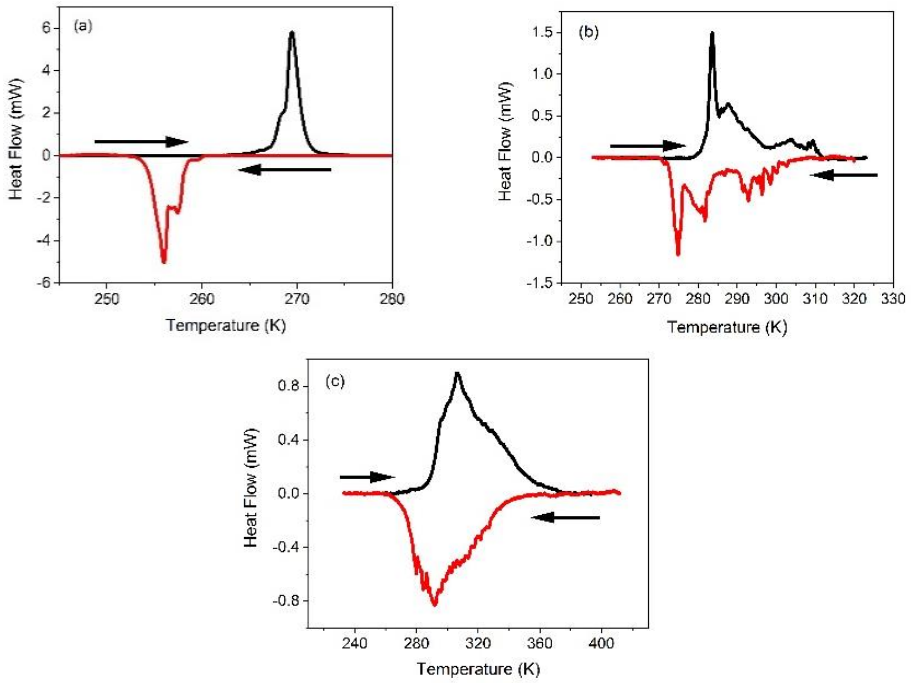

Figure 3.1 DSC measurement for cooling (red line) and heating (black line) for sample A(a), *B (b) and C (c)[6].*

Table 3.1 Heat and entropy of transformation (Q and S, respectively) for heating, h, and cooling, c, as well as the transformation temperatures.

Sample	M_s	M_f	Q_c	S_c	A_s	A_f	Q_h	S_h
Unit	K	K	J/mol	J/mol	K	K	J/mol	J/mol K
A	260	252	-257	- 1.00	264	273	256	0.95
B	305	272	-250	- 0.90	280	312	256	0.90
C	350	268	-240	- 0.80	267	367	248	0.80

They are a bit different for each sample, from the point of view of the peak width and shifting in start/finish temperatures of the transformation. In addition, the splitting and stepwise behaviour of the peaks show some diversity and dissimilarities. These are related to the well-known effect of change of the size and shape of samples, which - via creating nucleation centres differently - can also cause different fine splitting of the DSC peaks [46, 47]. *It worth mentioning that cycling for the first three heating/cooling cycles had no effect on the transformation temperatures.*

I calculated the heat and entropy of the transformation using Eqns. 2.1 and 2.2, respectively, and are presented in Table 3.1. They differ by a bit larger value than the error bar for sample C (the error bars are 5 as well as 3% for the heat and entropy of transformation, respectively) as compared to samples A and B. The average values of the transformation heat and entropy are $Q \cong 251$ J/mol and $S \cong 0.9$ J/molK, for the three samples on heating/cooling. This is in accordance with [5] for thermally induced transformation in my investigated alloy.

I constructed the hysteresis loop from the obtained DSC peaks, as defined in Eqns. 2.3 and 2.4: see Figure 3.2. The samples have hysteresis loops with different widths: **the dissipative energies**, evaluated as the area enclosed by the hysteresis loop, are 11.8, 2.0 and 7.0 J/mol for samples A, B and C, respectively. The fact that, the hysteresis up and down branches have different slopes for the three different samples indicate a difference in **elastic energies** contributions (see Chapter 1.4 and Eqn. (1.19)).

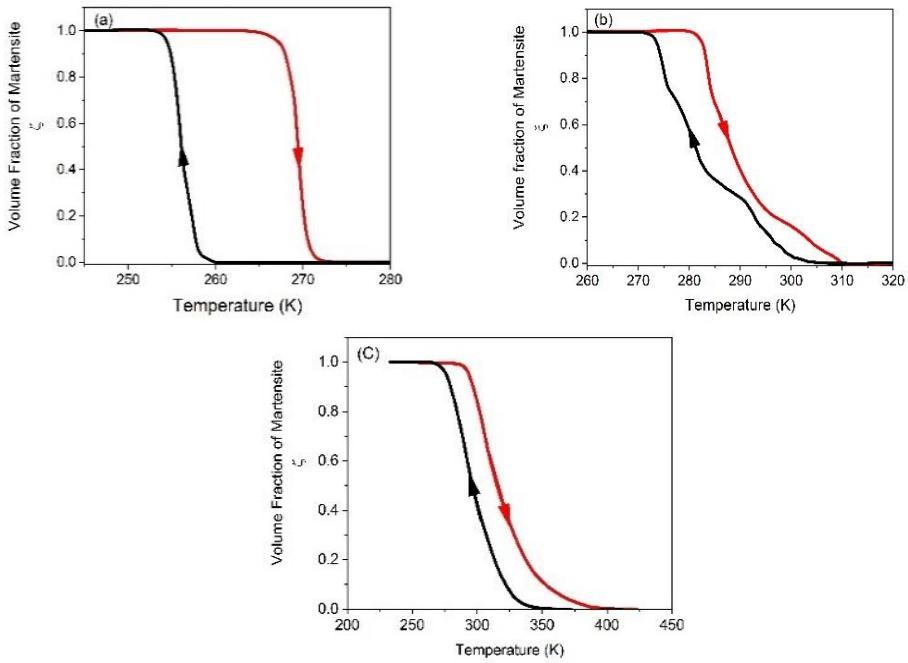

*Figure 3.2 Hysteresis loops for sample A (*a*), B (b) and C (c), the heating and cooling branches are represented by red and black lines, respectively [6].*

In addition, as it is also illustrated in Figure 3.2, there are steps on the up and down hysteresis branches (Figure 3.1b) indicating the stepwise character of the transformation.

I obtained the **AE emission** results simultaneously with the DSC measurements. The shape of sample B provides the best thermal contact with the DSC furnace and the step wise character is also strongly manifested at this scanning rate. Therefore, as an example, I show the AE results versus the temperature for sample B: see Figure 3.3. The AE activity peaks (the number of avalanches per unit time, dN/dt) and the jumps in the cumulative energy (E_{Σ} = ΣEi) are well correlated to the DSC peaks in Figure 3.1b. The AE activity is confined within the transformation temperature interval for both heating and cooling.

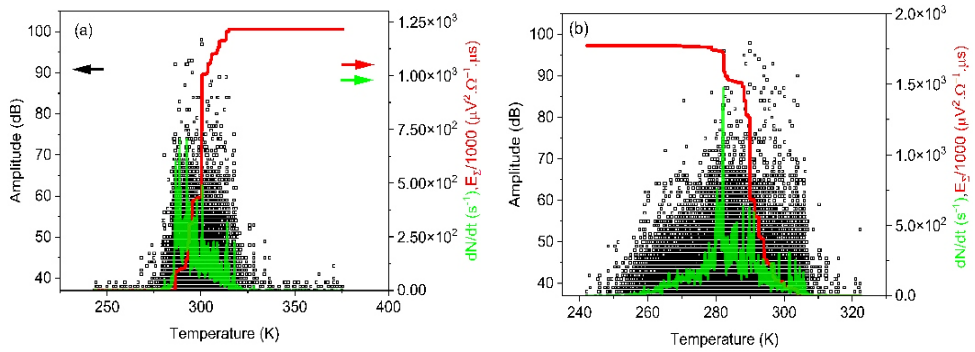

Figure 3.3 AE characteristics versus temperature for sample B. a*) heating, b) cooling. The scales for values of* $E_\Sigma = \Sigma E_i$ *are the same as those for dN/dt, after dividing by 1000) The squares correspond to amplitudes of hits, the continuous red and green lines show the cumulative energy (*$E_\Sigma = \Sigma Ei$*) and the acoustic activity [6].*

Figure 3.4 shows, the energy distribution functions of AE signals during heating and cooling for sample A. the fitting range was chosen visually for the linear part of the PDF however, it is still good to fit the whole range as my data has no clear cut off region (i.e. $exp\left(-\frac{x}{x_c}\right) \cong 1$, in Eqn.1.24), indicating the number of high energy hits became very low before the cut-off effect would be visible. The plots can be well approximated by straight lines over two-three orders of magnitude on the energy scale. The AE measurements were repeated 12 and 3 times for sample A and B, respectively, and exponents were the same within the error bars. The exponents of the distributions of energy, ε, and the maximum amplitude, α, as calculated from Eqn. 2.6 for samples A and B are shown in Table 3.2.

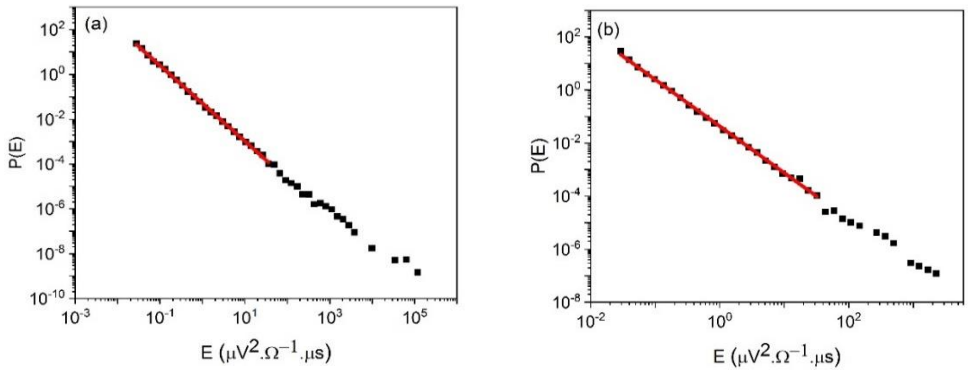

Figure 3.4 Energy distribution functions; Log P versus log E, obtained from acoustic measurements during heating (a) *and cooling (b) of sample A [6].*

Table 3.2 shows **ε, α**, N and E_t, for samples A and B. The error bars for α and ε are about ±0.3 and ± 0.1, respectively.

Sample	AE for Heating				AE for Cooling			
	N	$\boldsymbol{\alpha}$	$\boldsymbol{\varepsilon}$	E_t	N	$\boldsymbol{\alpha}$	$\boldsymbol{\varepsilon}$	E_t
A	18325	2.4	1.7	$8.18\text{x}10^3$	11623	2.7	1.7	$4.34\text{x}10^3$
B	31738	2.5	1.6	$4.76\text{x}10^4$	47834	2.6	1.6	$6.39\text{x}10^4$

It was observed in [5, 46] that the AE events have shown a certain asymmetry (e.g. the exponents for energy and amplitude or numbers of AE hits and cumulative energy are different for the forward and backward MT). In my study, I could not observe this asymmetry in the PDF exponents for heating and cooling, the results are the same within the error bars. Consequently, alternative method was considered to characterize the asymmetry in AE. This asymmetry can also be characterized by the relative change of N and E_t [22, 46] as follows:

$$\boldsymbol{\rho} = \frac{N_h - N_c}{N_c} \tag{3.1a}$$

$$\boldsymbol{\eta} = \frac{E_{th} - E_{tc}}{E_{tc}} \tag{3.1b}$$

The subscripts h and c refer to heating and cooling. The asymmetry is called negative if the sign of $\boldsymbol{\eta}$ and $\boldsymbol{\rho}$ is positive [5, 22, 46]: i.e. the asymmetry is negative if N or E_t is larger for heating. Table 3.3 shows my results for samples A and B. It can be seen that the numbers of hits and the total AE energy during heating is larger for sample A (the transition is more "noisy" for heating than for cooling), while the situation is just the reverse for sample B.

Table 3.3. Asymmetry exponents.

Sample	$\boldsymbol{\rho}$	$\boldsymbol{\eta}$	
A	0.58	0.88	negative asymmetry
B	−0.34	−0.26	positive asymmetry

3.1.1. Discussion of DSC and AE results

The different prehistories of samples A, B and C is revealed in small change, shift of the transformation temperature and change in the hysteresis, (see Figure 3.1 and 3.2 as well as and Table 3.1). In addition the elastic and dissipative energy contributions are also a bit different from each other. This can be attributed to the possible variation in the size and distribution of γ-phase precipitates like it was also mentioned in refs. [5, 22, 38, 46]. The fact that the exponents have almost the same values in Table 3.2 is in accordance with the results of [5, 22], in which a similar behavior was observed in $Ni_{49}Fe_{18}Ga_{27}Co_6$(at.%) single crystals, with different γ-phase precipitates (see the Table 3 in [5]). This can be related to the robustness of the characteristic exponents against microscopic details, if the mechanism is the same. For instance, according to Ref. [31] the energy exponents for martensitic transformations with different martensite structures (from orthorhombic to tetragonal structures) vary only between 2.0 and 1.6. On the other hand, the most interesting difference observed in ref. [5] was that the samples with different γ-precipitates had different asymmetry. Thus, the asymmetry parameters are more sensitive for the microscopic details of phase transformation.

The most important new result of my work is related to the excellent agreement between the simultaneously measured DSC and AE signals (see Figure 3.3). The AE parameters and especially the E_Σ and activity, $\frac{dN}{dt}$, curves correlate very well with the stepwise DSC curves. This is a nice illustration, that the stepwise DSC branches are fingerprints of the intermittent motion of the interfaces during MT. The jumps of the interfaces are accompanied with local changes of the elastic strain, which results in emission of AE avalanches. This emission is also a special kind of elastic energy relaxation and the energy of elastic waves dissipates during their propagation.

Furthermore, on the basis of my result, an analysis of the experimentally observed average temporal shape of avalanches at fixed area could also be carried out. This also leads to a deeper understanding of the well-known AE enigma problem.

3.1.2. Enigma problem of AE results

I investigated the power law scaling relations between AE parameters: E $\sim A^{\chi}$ and S $\sim A^{\beta}$ for thermally induced MT for heating of sample B, see Figure 3.5 (I will explain the fitting range in Chapter 3.1.3 below). I made the fitting for the data averaged by logarithmic binning. For example, E_{AE} is averaged for fixed bins of A_m in Figure 3.5a. I investigated the different correlations between AE parameter using similar binning, in which the bins, number and width, are selected according to the parameter on x-axis. Table 3.4 contains the values of the above exponents.

The self-similarity of crackling noise implies that the above power relations between the AE parameters exist as well (see: Chapter 1.5 and Eqn. (1.31-1.33)). The MFT provided a theoretical estimate for the characteristic exponents of correlations between crackling noise parameters. However, the exponents obtained in Table 3.4 do not agree with the MFT results where β and χ should be 2 and 3, respectively. This was valid in general for numerous AE measurements for different sources of crackling noises and called "enigma" for AE results [3]. Understanding this 'enigma' is crucial as it could lead to refined theoretical models that better capture the behavior of AE and noise behavior in different materials.

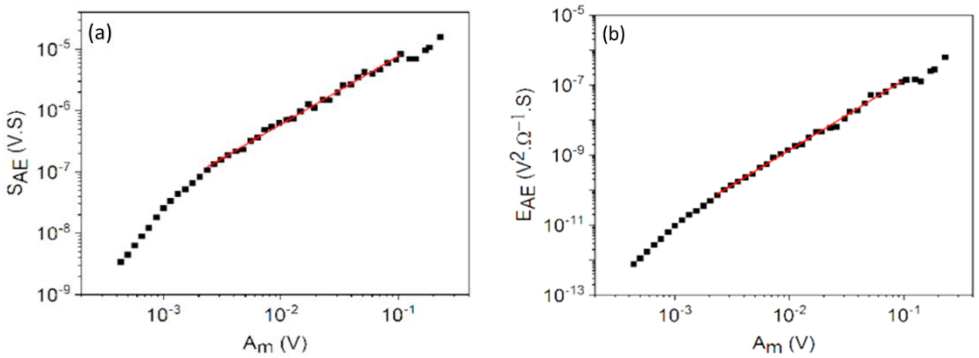

Figure 3.5. Relations between Log S_{AE} versus Log A_m (a) *Log E_{AE} versus Log A_m(b) for sample B on heating [4]. In this figure S_{AE} and E_{AE} are the detected area and energy, respectively. A_m is the maximum amplitude.*

Table 3.4 the exponents of the scaling relations

χ	β
2.00 ± 0.08	1.11 ± 0.05

3.1.3. Introducing of new scaling parameter *(φ)*

In order to resolve the above mentioned enigma, we have investigated the original theoretical prediction for the source function of the average temporal shape of avalanches, $V(t)$, at fixed area and searched for appropriate parameters being proportional to the non-universal/material dependent constants a and τ_s [4]. Let us start from the averaged source function at a fixed area, as it was already introduced by Eqn. (1.38):

$$V_{av}(t) = ate^{-(\frac{t}{\tau_s})^{\delta}} \tag{3.5}$$

where $\delta = 2$ in MFT, and we assume in the following this value for δ. It can also be seen that τ_s is the characteristic time of the avalanche decay [3]. It was suggested by [3] that the maximum amplitude and the corresponding time, so-called rising time (t_m), are less polluted by the transfer problems. Indeed, by setting $\frac{dV(t)}{dt} = 0$, the maximum of Eqn. (3.5) can be obtained as:

$$t_m = \frac{\tau_s}{\sqrt{2}} \tag{3.6}$$

and

$$V_m = a\, t_m\, e^{-\frac{1}{2}} = B\, t_m \tag{3.7}$$

From Eqn. 3.7, we can find that V_m and t_m are linearly related to each other if *a (*or *B)* is constant [3], In general *B* (or *a*) is not constant and we describe this by allowing that the $B=\frac{V_m}{t_m}$ parameter can be dependent on V_m as [4]:

$$B \sim V_m^{\varphi} \tag{3.8}$$

This conjecture, suggested by our team, is supported by the general self-similarity, which means invariance on stretching the scale of a given variable, x: $f(x) \propto f(\lambda x)$, and only the power function provides this property, i.e. $x^{\mu} = (\lambda x)^{\mu} \sim x^{\mu}$). This means that, in general instead of a linear relation between V_m and t_m, we can assume [4].

$$V_m^{1-\varphi} = a\, t_m. \tag{3.9}$$

Thus, once **the constancy of** φ has been proved (at least for a given similarity class), dividing V by V_m and t by $t_m \sim V_m^{1-\varphi}$ in Eqn. (3.5), a universal function should be obtained as

$$V^*(t^*) = e^{\frac{1}{2}}\, t^*\, e^{-(\frac{t^*}{\tau^*})^2} = 1.65 t^*\, e^{-(\frac{t^*}{\tau^*})^2}, \tag{3.10}$$

where the dimensionless (universal) parameters are given as $V^* = \frac{V}{V_m}$, $t^* = \frac{t}{t_m}$ and $\tau^* = \frac{\tau_s}{t_m} = \sqrt{2}$. It has to be noted that the mean field results can only be obtained if $\varphi = 0$ (see also below in Chapter 3.1.4.)

It should be noted that, on the basis of the self-similarity [29] it is indeed expected, that the normalized $V_{av}(t)$ functions should fall on a common curve for different bins of S using one scaling parameter only (there should exist a power relation between the possible scaling parameters). Thus, based on the power relations predicted by MFT (i.e. $S \sim A^2$ as well as $D \sim A$) dividing both $V_{av}(t)$ and t axes by $S^{0.5}$ or by A [48-50] it can be expected that universal temporal shapes should be obtained, but the curves did not scale completely in a universal way [4, 49-50].

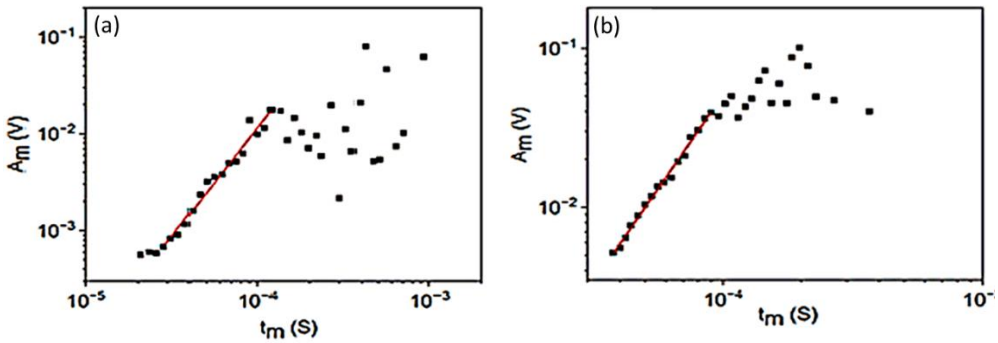

Figure 3.6. Log A_m (A_m is the experimental value of V_m) versus log t_m plots for heating in my sample B (a) *(at B = 0) [4], and for cooling in alloy $Ni_{45}Co_5Mn_{36.6}In_{13.4}$ (b) at small, constant, external magnetic field (B = 250 mT). Fig. b was constructed from experimental data of N. Samy [51] published also in [4].*

On the other hand, as I will show below, our proposal for scaling provides nice, scaled together temporal shapes. Before doing this, I have to discuss the experimental determination of the values of φ and the experimental problems related to the finite threshold values and signal distortions due to the signal transfer effects.

3.1.4. Experimental validation

Regarding **the determination of** φ, let us use the Eqn (3.9) first, since according to the analysis of [3] the V_m and t_m parameters are not distorted by the above experimental difficulties. The fulfillment of the power relation in form of Eqn. (3.9) is illustrated in Figure 3.6a and Figure 3.6b, where it can be seen that the fitting can be made from the beginning up to an upper window (see below the comments on fitting window). Another possibility for the determination of φ is from the scaling exponents of E versus A or S versus A relations as follows. The reduced area of the avalanche is given by

$$S^* = \frac{S}{V_m t_m} = \int_0^{T^*} V^*(t^*)dt^* = 1.65\frac{\tau^{*2}}{2}\left(1 - e^{-(\frac{T}{\tau_s})^2}\right) \qquad (3.11)$$

$$=1.65\ (1 - e^{-\frac{T^{*2}}{2}}).$$

Now, we can calculate the reduced duration time from experiments as the difference of the start and finish times (t_s and t_f, respectively) given by a fixed threshold value, C, from Eqn. (3.10)

$$ln\frac{C}{V_m} = ln1.65 + lnt^* - \frac{t^{*2}}{2}. \qquad (3.12)$$

It is clear that there are two solutions, belonging to the start and finish times:

$$t_s^* \cong \frac{C}{1.65V_m}, \qquad (3.13)$$

$$t_f^* \cong \sqrt{2ln\frac{V_m}{C}} \qquad (3.14)$$

Thus, we have

$$T^* = t_f^* - t_s^* = \sqrt{2ln\frac{V_m}{C}} - \frac{C}{1.65V_m} \cong \sqrt{2ln\frac{V_m}{C}}. \quad (3.15)$$

For $\frac{C}{V_m} = 10^{-4}, 10^{-3}, 10^{-2}, 10^{-1}$, the first term is 4.3, 3.7, 3.0, and 2.1, respectively, i.e., neglecting the $\frac{C}{1.65V_m}$ term is reasonable. It is also worth noting that the duration time or its reduced value goes to an asymptotic limit as C goes to zero. Now, using that $\left(1 - e^{-\frac{T^{*2}}{2}}\right) = 1 - \frac{C}{V_m}$, from Eqn. (3.11) we get

$$\frac{\partial lnS}{\partial lnV_m} \sim 2 - \varphi, \quad (3.16)$$

if $\frac{C}{V_m} \ll 1$. Similarly, it can be shown that

$$\frac{\partial lnE}{\partial lnV_m} \sim 3 - \varphi, \quad (3.17)$$

(see also the Appendix).

Eqns. (3.16) and (3.17) connect the AE enigma problem to the relation between the two non-universal factors, a and τ_s, present in the theoretical expression in Eqn. (3.5). As we have seen they are related to the maximum of *V(t), V_m*, as well as to the rising time (t_m=*R)* and we demonstrated from our experimental data that they are related by a power relation.

Since in the next Chapters the value of φ will also be used for creating universal scaled (normalized) average temporal avalanche shapes, its value will be always an average of data estimated from the power relation between V_m and t_m, as well as from Eqns. (3.16) and (3.17), see also Table 3.5.

In AE experiments, the measured signal does not really reflect the real source function [3,52] (see also Chapter 2.4.2). The signal can always be distorted due to various effects which are called **transfer problems**. **First**, there is a problem of the transmittance of the waveguide, sensor, and amplifier, (i.e. the detection system). This can lead to limitations for simultaneously detecting more than one avalanche. As a result, overlapping or diminishing of

Table 3.5 Values of φ calculated from different relations for alloy A and B, respectively. It can be seen that they are very similar, and the average value for the two alloys is $\varphi \cong 0.74 \pm 0.10$ [4].

Equation	Value of φ	
	$Ni_{45}Co_5Mn_{36.6}In_{13.4}$	$Ni_{49}Fe_{18}Ga_{27}Co_6$
(3.9)	0.6 ± 0.1	0.6 ± 0.1
(3.16)	0.8 ± 0.1	0.90 ± 0.08
(3.17)	0.9 ± 0.1	1.0 ± 0.1
Average	0.77 ± 0.11	0.83 ± 0.13

more than one avalanche (i.e. a long-lasting avalanches may stop shorter ones or concatenate long trains of avalanches that stared before the end of the first one) [49,52]. In addition, the misspecification of the threshold, C, can also results in diminishing of the signals with low amplitude [3, 4, 52]. **Second**, there is always a macroscopic vibration of the sample + detector system (with a certain frequency w), which is called "ringing effect" [3]. Thus, the detected AE signal is the convolution of the source signal and the transfer function can be taken as a form of damping oscillation [3, 48, 53] as follows;

$$T(t) = \cos(wt)e^{-\frac{t}{\tau_a}}. \qquad (3.18)$$

τ_a is the characteristic decay time of the propagating acoustic elastic wave. As a result, it was concluded in [3] that the AE spectrum does not represent the temporal shape of avalanches nor the model predictions, (see also the discussion on the normalized average shape of avalanche).

I carried out the following analysis [4] to minimize the transfer distortions on the detected exponents in the relations between directly measured AE parameters (detected AE are denoted below by A_m and D, while V_m and T are used for the source signal parameters). It was taken into account that the transfer effects can dramatically distort the value of D.

Indeed, in accordance with [30, 52], it can be shown that D≅T if $\frac{\tau_a}{T} \ll 1$ and $\frac{C}{A_m} \ll 1$ [4, 52-53]. Indeed it is clear from Figure 2.7b in Chapter 2.5. that for $\frac{\tau_a}{T} \ll 1$, (if $\frac{C}{A_m} \ll 1$ is also valid) the transfer distortion is negligible. Similarly, at constant (but small) $\frac{\tau_a}{T}$ ratio, for small $\frac{C}{A_m}$ the evaluated duration time asymptotically approaches to its limit, i.e. D≅T. The above conditions give a lower bound for fitting the experimental power relations only above a certain D and/or A_m values in a given experiment (where τ_a and C are constants). Thus, we can write that [4];

$$\frac{\partial ln\frac{T}{D}}{\partial lnA_m} = \frac{\partial \ln T}{\partial lnA_m} - \frac{\partial lnD}{\partial lnA_m} = 1 - \varphi + \frac{1}{2ln\frac{A_m}{C}} - \theta, \qquad (3.19)$$

where the first three terms arise from Eqns. (3.15) and (3.9). θ represents the reciprocal value of the slope of the lnA_m versus lnD (see Figure 3.7). Thus θ can be used as an experimental parameter characterizing the transfer effects; for $\theta = 1$ these are neglected (if $\frac{A_m}{C}$ is also large). Figure 3.7 shows that the slope of the relation between $\log A_m$ and logD relation, has a "half-moon" shape [3-4], the slope of fitting in the linear region is 1.9 ± 0.1, which provides $\theta = \frac{1}{1.9} = 0.6 \pm 0.1$, indicating that even in the fitted region $\theta \neq 1$. We have seen that, related to the lower bound of the fits as suggested above, at least linear relations e.g. between log D and log A_m can be

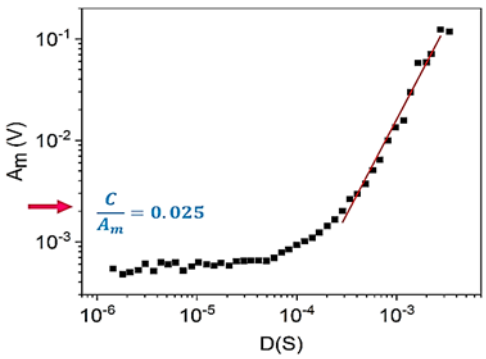

Figure 3.7. Relation between the log A_m ~ log D, $\frac{C}{A_m} = 0.025$ is indicated on the vertical axis on the log A_m vs log D plot[4].

obtained, even if the slope of this is different from the expected, undistorted value θ=1.On the other hand, is also expected that at large values of A_m (or D) possible overlaps of avalanches (some sub-avalanches can be merged and thus the duration time will be distorted, i.e. will be longer, by this reason) can be disturbing and/or too small numbers of events can lead to large scatter of the points (e.g. see the plots in Figure 3.6 at large t_m values). This leads to a recommended upper bound for the fit. Thus, when choosing properly the centre of the window of fit on the log A_m axis and keeping it fixed for the different scaling plots, the value of θ, can be kept constant. Thus, one obtains that the conclusions drawn from different experimentally determined scaling exponents in Eqns. 3.6 and 3.7, providing the same φ value are in good agreement with each other.

All the correlations were investigated keeping the values of θ constant. This was done through choosing the proper fitting window on the log A_m axis. Figures 3.5, 3.6 and Figure 3.7 illustrate well the chosen widow of fit.

Before closing this section, it is worth mentioning that the most frequently considered scaling relation is $S \sim D^{\gamma}$, from which the value of γ was usually calculated and, most frequently, a value less than the MF value, 2, was obtained. Thus, Figure 3.8 shows the $logS$ versus $logD$ plot in alloy B for heating. The slope is sensitive to the window of fit: its value, fitting between 0.2 ms and 3.0 ms, (the red line in Fig. 3.8) is γ=2.14±0.17. However, including points belonging to smaller and smaller values of D, the value of γ

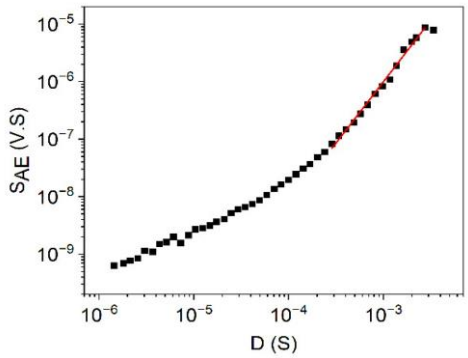

Figure 3.8 the scaling relation log S versus log D for heating of sample B [4].

gradually decreases. The $\gamma \cong 2$, corresponds to the same window of fit used in the previous figures: this illustrates, besides the good agreement of the scaling exponents with each other, that the value of γ consistent with a $\gamma \cong 2$ MF value could be obtained.

3.1.5. Normalized average temporal shape of avalanches

For the construction of averaged temporal shapes we divided the S scale into seven intervals (S-bins) and created the averages of the *normalized avalanche versus time functions* within each bin. In Figure 3.9a, the voltage and time axis are normalized by A_m following the assumption that [3-4] $A_m \sim t_m$: we can see that the curves do not fall on a common curve. On the other hand, in Figure 3.9b, we consider the correction term φ and using Eqn. 3.9: the curves are scaled much better together (see the insert too), especially in the first, fast-decaying part of the curves [4].

From Figure 3.9, it can be seen that curves belonging to the two first bins (at small values of the fixed area) as well as to the last two bins show some deviation/scatter from the common curve shown in the insert. This can

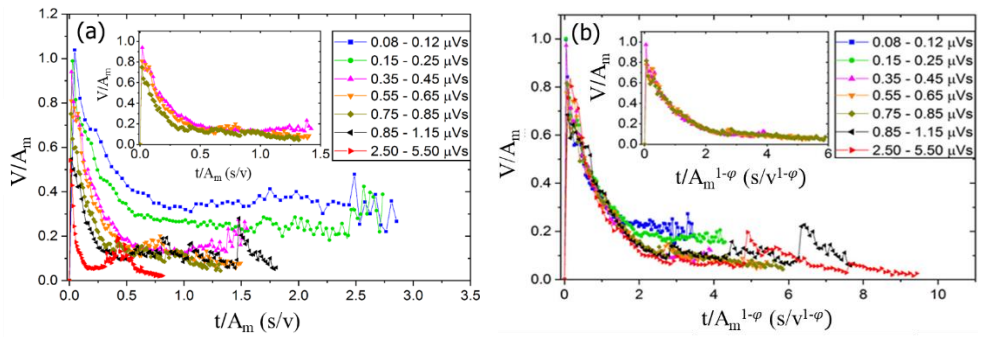

Figure 3.9. Normalized functions $V^*(t^*)$ obtained by scaling: the voltage and time with A_m (a) *and the voltage with A_m and time scales with $A_m^{1-\varphi}$ for heating in alloy B (at B = 0) at different bins of avalanche area. The insets represent the scaling of avalanches within the selected bins of avalanche area [4].*

be due to the distortions caused by the transfer and threshold effects (at small values of S) as well as to some overlaps of the large avalanches (for large, fixed values of S). Thus, we have shown that using the recognized power (but not linear) shapes can be well scaled together for a universal function using the parameters A_m and exponent φ.

3.2. AE during anomalous stress-strain curves and burst like transition along [110] direction

Now, I turn to the second part my thesis which is the investigation of **anomalous stress-strain curves** during stress induced MTs**.** These are important in understanding the mechanism of MT and controlling the functional properties of SMAs. For example, production of rubber like behaviour from SIM-aged samples [16, 39], see also chapter 1.4. In addition, they are rich with structural changes information. These made them typical for acoustic emission investigation and more interesting/challenging for phenomenological discussion. My investigated alloy has two anomalous behaviours upon compression along [011]. as I will show in the following sections.

3.2.1. Complete anomalous super-elastic cycles under compression

I investigated **the compression stress strain curves** at five different temperatures 383, 393, 403, 413 and 353K for sample C, with strain rate 0.0017 s^{-1}. Above, 353 K, closed anomalous super-elastic loops were observed (see Figure 3.10). These curves are anomalous in the sense that the loading branch shows an overall negative slope where local sharp stress drops exist. On the other hand, the unloading branch there is first sharp jumps (with an audible click) which can be sometimes followed by a small jump (with/without audible click), The dissipative energy calculated as the area enclosed by (σ - ε) hysteresis was about 35 J/mol

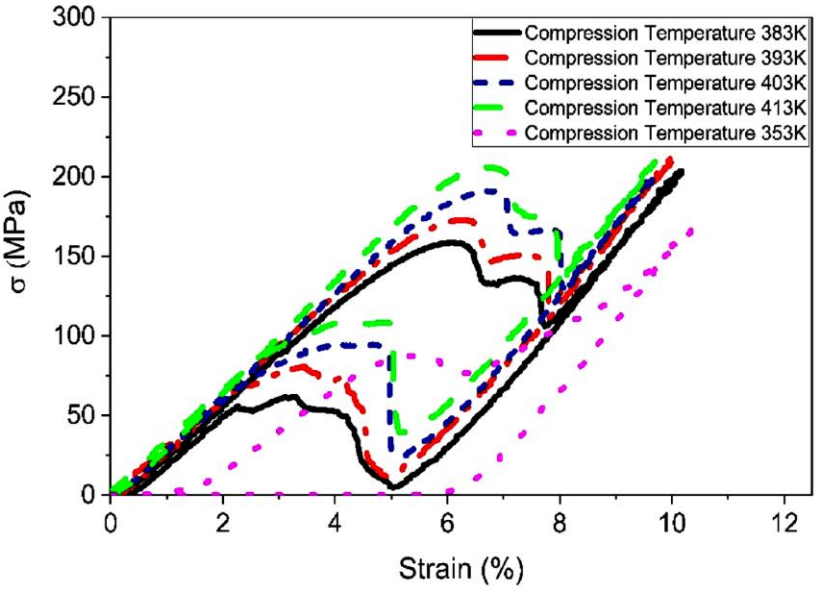

Figure 3.10 Stress-strain curves during compression along the [110] axis: sample C at different temperatures. The curves were taken subsequently between 383K and 413 K, starting at 383 K, while the curve at 353K was taken after the above runs [6].

The AE measurement were taken simultaneously for loading/unloading at 383K. In this section I will consider the $\sigma - t$ plots instead of $\sigma - \varepsilon$ curves, in order to show the correlation with the acoustic signals (hit mode), as shown in Figure 3.11a: this implies a dynamic measurement with a constant rate. For a better qualitative visualization, I created Figure 3.11b, to compare the evolution of acoustic emission hits (N = $\sum_i N_i$, $\frac{dN}{dt}$) with the $\sigma - t$ curve. **For loading:** an increase in AE activity is observed along the first, almost linear part elastic region of A-phase, with increasing/high number of hits, N. At the first stress drop a decrease in $\frac{dN}{dt}$ is observed and there are practically no signals after the second stress drop, i.e. in the elastic region of M-phase. **For unloading:** there are signals before the first stress jump and there are also AE events even during the last part, which has a similar average slope as the first (austenitic) part of the loading curve. The results were repeated for 3-times at this temperature with the same observations.

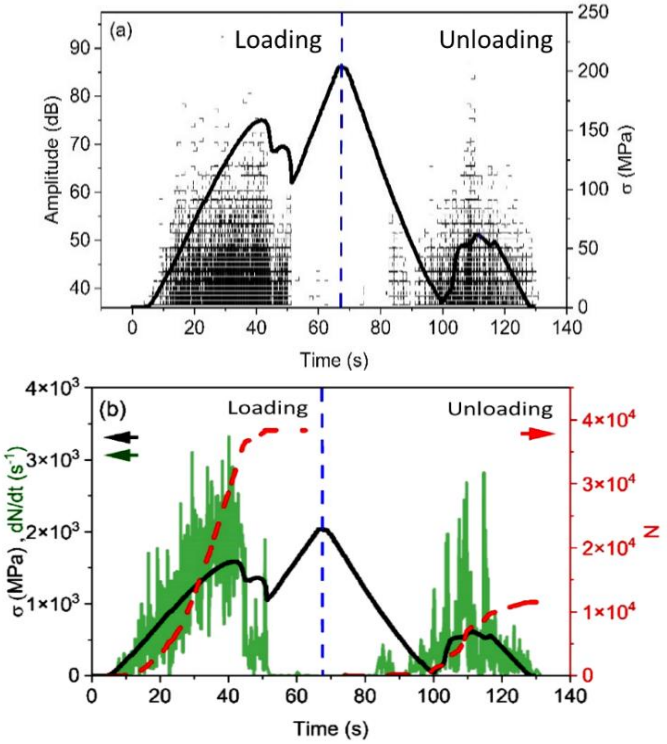

Figure 3.11 Acoustic signals and the stress versus time curves for sample C: (a) *during loading and unloading. b) shows the cumulated number of signals (dashed red lines), the AE activity (dN/dt) (in green) as well as the stress curves (in black) for loading and unloading at 383 K (the maximum of the stress curve corresponds to 200 MPa, in accordance with* a)*[6].*

Figure 3.12 show the PDF for energy and the corresponding maximum likelihood fit (MLE), the plateau region corresponds to the critical exponents dashed by red line. Table 3.6, shows the amplitude and energy exponents (the values for loading and unloading are the same within the error bars), as well as, the values for N and E_t. These exponents are similar to the exponents shown in Table 3.2 for thermally induced transformation within the error bars, at the investigated rate of deformation.

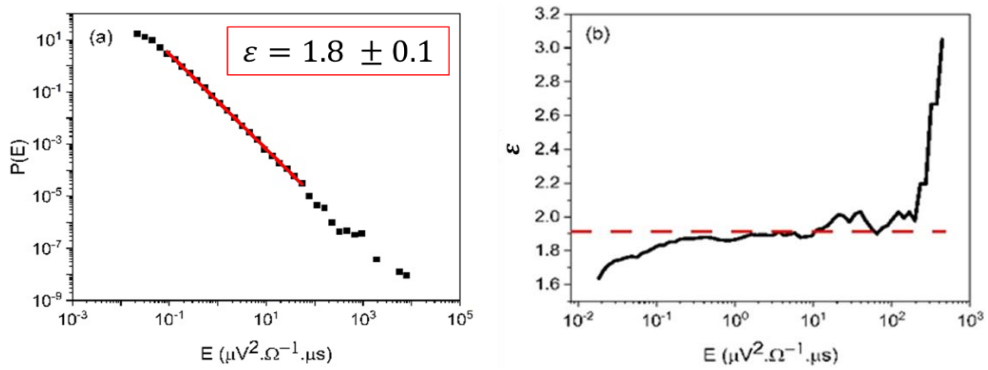

Figure 3.12 Energy distribution functions for sample C; Log P versus log E, obtained from acoustic measurements during loading (a) at 383 K and the maximum likelihood fit (b) (the dashed line shows the value obtained from the fit, indicated by the straight line, in a): see also the text) [6].

Table 3.6 shows $\boldsymbol{\varepsilon}$, $\boldsymbol{\alpha}$, *N and* E_t, *for sample C during stress induced MT. The error bars for* α *and* ε *are about* ± 0.3 *and* $\pm$ *0.1, respectively.*

Sample	Loading				Unloading			
	N	$\boldsymbol{\alpha}$	$\boldsymbol{\varepsilon}$	E_t	N	$\boldsymbol{\alpha}$	$\boldsymbol{\varepsilon}$	E_t
C	38346	3.0	1.8	2.07×10^5	11518	2.8	1.8	2.77×10^4

The different values of N in Figure 3.11b and Table 3.6 during loading and unloading demonstrate the asymmetry of the transformation. The asymmetry parameters are given in Table 3.7. The positive asymmetry means that the total elastic energy relaxed during forward/loading transformation is larger than the total elastic energy relaxed backward/unloading transformation i.e. the loading branch is more "noisy" than the unloading one.

Table 3.7 the Asymmetry parameter for the stress induced MT.

Sample	$\boldsymbol{\rho}$	$\boldsymbol{\eta}$	
C	-0.70	-0.86	positive asymmetry

Figure 3.13, as an illustration, shows the scaling relations between E and A as well as S and A for loading/unloading for stress induced MT. Table 3.8 shows the scaling exponents for loading and unloading. It can be seen that $\varphi \neq 0$, i.e. the enigma for AE still exist even for stress induced transformations as well.

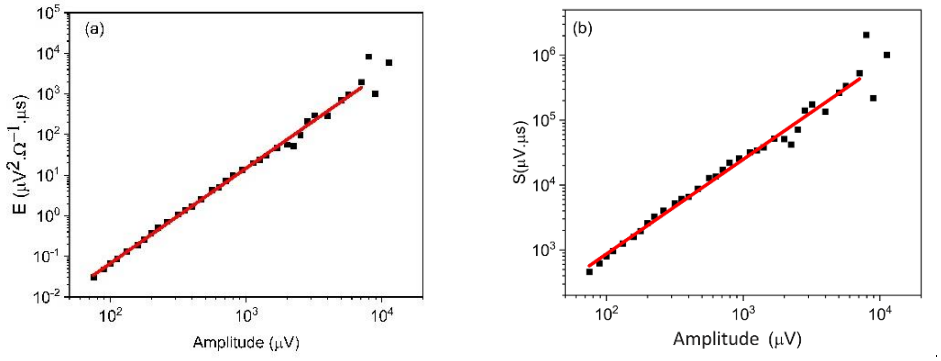

Figure 3.13 Scaling relations between the AE parameters for sample C; (a) E versus A and (b) S versus A for loading [6].

Table 3.8 power exponent for the scaling relations.

	χ	β
Loading	2.3± 0.3	1.5±0.1
Unloading	2.3± 0.2	1.4±0.2

3.2.2. Compression cycle resulting in residual martensite

An additional anomaly is observed in the unloading behaviour of the sample A. The sample was compressed along [011] orientation with strain rate 0.003 s^{-1} at temperatures 283 and 293K ($> A_f$, where A_f, is the usual austenite finish temperature for thermally induced transformation), see Figure 3.14

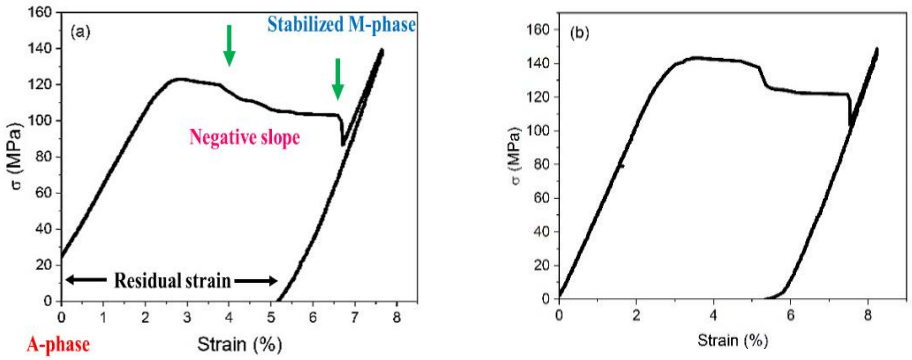

Figure 3.14 The stress-strain curve for sample A compressed along [011] at 283K, the green arrows indicate the stress drops and 293K(b)[6].

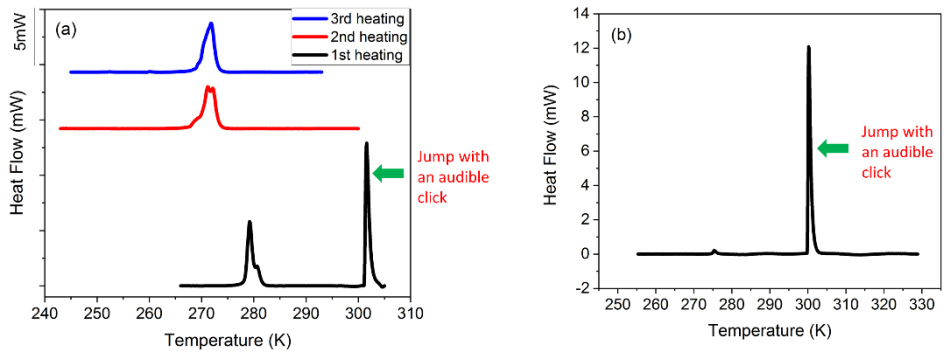

Figure 3.15 the DSC peak for burst strain recovery,1st heating, compared to heating peak of the thermally induced MT,2nd and 3rd heating, at 283K (a) *the burst strain recovery after compression at 293K(b). The green arrows indicate the burst peak [6].*

The stress- strain curve is anomalous in the sense that during loading: the plateau region has an overall negative slope with two stress drops (as expected from the results of the previous chapter 3.2.1). On the other hand during unloading: the sample remained in M-phase with residual strain ~6%, see Figure 3.14a and 3.14b. *Furthermore, the fact that the sample remained in the M-phase indicates the formation of stabilized martensite structure.* I transferred sample A after compression at 293 K for **DSC investigation** and the 6% residual strain was fully recovered after a sudden jump with an audible click during heating: see Figure 3.15a and 3.15b. The recovering behaviour was accompanied by sharp and narrow endothermic peak in the DSC curve at a temperature higher by ~35K than A_f for the thermally induced transformation. This peak indicates the so-called burst behaviour and it represent the temperature at which the compressed sample has an explosive/burst strain recovery during heating [6]. Nevertheless, heating the sample after the compression at 283 K (in Figure 3.12a,1st heating), a smaller and wider peak was also observed only by ~ 10K higher than the temperature of the thermally induced M → A transformation. This indicates that the stress induced martensite had two transformation temperatures, i.e. it contained two different martensite modifications [54] (see also the discussion below).

The summary of DSC results obtained on sample A are given in Table 3.9. The units of the heats and entropies of transformations here (in contrast to data

Table 3.9 Summary of the DSC results obtained during: thermally induced MT without compression (I), thermally induced (burst like) after compression at 283K (II) and thermally induced (burst like) after compression at 293K (III). The lower index c and h are for cooling and heating, respectively. The question marks indicate that we had a problem in the sudden change of the baseline and the estimated values are less reliable.

MT	q_c	q_h		s_c	s_h		T_{pc}	T_{ph}	
	J	J		J/K	J/K		K	K	
I	0.0673	0.0670		0.000261	0.000248		256	269	
II	-	*h1*	*h2*	-	*h1*	*h2*	-	*h1*	*h2*
		0.0530	0.0674 ?		0.000190	0.000223 ?		279	302
III	-	-	0.0615	-	-	0.000205	-	-	300

given in Table 3.1) are given in units J as well as J/K and denoted by q and s, respectively. T_{ph} and T_{pc} are the peak positions for heating and cooling, respectively.

The lower index h_1 and h_2 represent the first and second peaks in the first heating run in Figure 3.15a. while the lower index h is used for the thermally induced MT, as shown in Table 3.1. Also, using the sample A, with mass m=1.6 x10^{-5} kg that correspond to a molar mass M=0.0612 kg/mol, the heat and entropy of the transformation for the burst like recovery was calculated from the peak shown in Figure 3.15b; Q_b=235J/mol and S_b = 0.78 J/mol.K, (the lower script b is used for burst), respectively. It can also be seen from the Tables 3.1 that $S_h > S_b$(by about 10 %) in accordance with [56-58].

AE emission results taken simultaneously with the DSC measurements as the function of temperatures for sample A, during burst-like recovery after compression at 283K is shown in Figure 3.16. It can be seen that $\frac{dN}{dt}$ peaks and the jumps in E_Σ are well correlated with the DSC peaks in Figure 3.15a for 1st heating.

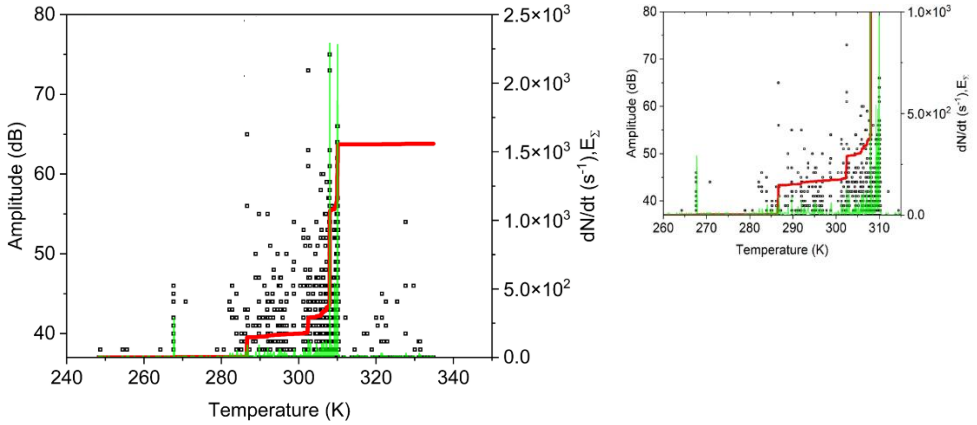

Figure 3.16 AE amplitudes as well as numerical values of the AE activity and cumulative energy versus temperature. (The given units on the right-hand vertical axis are the same for both dN/dt and E_Σ, i.e. the scales are identical: see also the enlarged part on the right [6].

Figure 3.17 shows the PDF for energy for the burst like transition. Table 3.10, contains the exponents E, A and the cumulative number of energy, E_t, and hits, N. Again, the exponent are the same as Table 3.2 and Table 3.6 within the error bar, however a large decrease in the number of hits is observed.

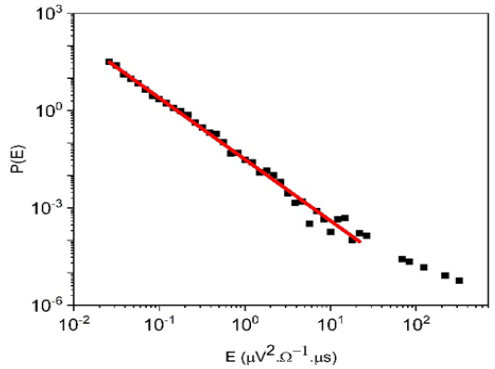

Figure 3.17 P(E) for the burst like transition of sample A from first run after compression at 283 K [6].

Table 3.10. $\boldsymbol{\alpha}$,$\boldsymbol{\varepsilon}$, N and E_t for burst-like transition, with the same error bar as Table 3.2.

Sample	AE for Heating			
	N	$\boldsymbol{\alpha}$	$\boldsymbol{\varepsilon}$	E_t
A (Burst)	2823	3. 0	1.9	1.56×10^3

3.2.3. Discussion

3.2.3.1. Interpretation of the anomalous stress-strain curves

In $Ni_{49}Fe_{18}Ga_{27}Co_6$ single crystal twinned martensite, TM, can be produced by the thermally induced MT, as it is typical for thermally induced transformations in general, while for stress induced MT detwinned martensite develops. In addition the $(\sigma - \varepsilon)$ curve can be quite anomalous for specific crystallographic orientations. For example; the $(\sigma - \varepsilon)$ along [001] and [011] orientations had shown normal as well as anomalous super elastic curves upon compression, respectively [20, 59-60]. The anomalous behaviour in the loading curve is explained by the possible (competing) nucleation and growth of the two martensitic structural modifications (twinned as well as detwinned martensites, TM and DM, respectively). On the basis of this the following interpretation can be given [7]: the TM nucleates first (if the martensite start stress is larger for DM: $\sigma_s^{DM} > \sigma_s^{TM}$, see Figure 3.18), and at a certain martensite volume fraction, ξ_c, during the normal increasing stress-strain branch, DM suddenly nucleates. Using the results of ref. [61] the stress drop, $\Delta\sigma$, can be given as:

$$\Delta\sigma = - (\varepsilon^{tr\,DM} - \varepsilon^{tr\,TM})\, \mathcal{S}(\xi_c)\, \xi_c \qquad (3.21)$$

Where $\varepsilon^{tr\,DM}$ and $\varepsilon^{tr\,TM}$ are the transformation strains and $\mathcal{S}(\xi)$ is the effective stiffness of the TM + A two-phase system [7]. The stress drop is negative if $\varepsilon^{tr\,DM} > \varepsilon^{tr\,TM}$ and $\sigma_s^{DM} > \sigma_s^{TM}$ first of all because the nucleation energy of DM is larger than for TM. After the stress drop the process can be repeated in two different ways: i) for large stress drop, leading stress below σ_s^{TM}, the system falls to the elastic regime, and the further growth starts with the slope $\mathcal{S}(\xi_c)$, or ii) for moderate stress drop, the dropped stress is above σ_s^{TM}, the TM martensite continues its growth, and the process continues/repeats.

On the basis of the experimental results obtained in chapter 3.2.1 and 3.2.2, it can be mentioned that: the final formed stress induced martensite upon compression along [011] orientation has a ***stabilized martensite structure, DM, and its formation is accompanied with a sudden change in strain fields***

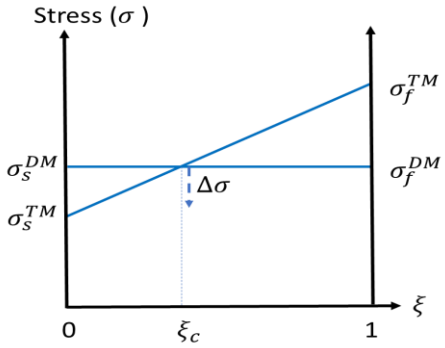

Figure 3.18 Schematic representation for the stress verses martensitic volume fraction [7].

causing stress drops. However, the dissolution of DM is always accompanied by jumping behaviour, sudden change in strain fields, observed for sample A in the burst strain recovery and sample C in the local jumps of the unloading curve.

We have seen in Figure 3.15 that $\Delta T = T_p^{DM\to A} - T_P^{TM\to A} > 0$. This shift, can be estimated from the Q and S values, For sample A (from Table 3.9), we get that, $\frac{Q_b}{Q_h}$ = 0.92 and $\frac{S_b}{S_h} = \frac{s_b}{s_h}$ = 0.83, while for sample C (from Table 3.1) $\frac{Q_b}{Q_h}$ = 1.03 and $\frac{S_b}{S_h}$ = 0.88 is obtained. Furthermore, using the approximate relation for the peak temperatures $T_P \cong$ Q/S we have:

$$\frac{\Delta T}{T_P^{TM\to A}} = \frac{T_p^{DM\to A}}{T_P^{TM\to A}} - 1 = \frac{Q_b S_h}{Q_h S_b} - 1 \qquad (3.22)$$

From Eqn. 3.22, using $\frac{Q_b S_h}{Q_h S_b}$ from the above calculated ratios ($\frac{Q_b}{Q_h}$ and $\frac{S_b}{S_h} = s\frac{s_b}{s_h}$), $\frac{\Delta T}{T_P^{TM\to A}}$= 0.11 and $\frac{\Delta T}{T_P^{TM\to A}}$ = 0.16 are obtained for sample A and C, respectively. Now, $\frac{\Delta T}{T_P^{TM\to A}}$= 0.12, and $\frac{\Delta T}{T_P^{TM\to A}}$= 0.14 for sample A and C, respectively from the measured ΔT values. Therefore, the measured and estimated values are in good agreement, taking also into account the error bars.

From the results of the first heating for the sample compressed at 283K the wider peak observed at the temperature slightly higher than the thermal

transformation is attributed to the transformation of TM →A, the second peak and the first heating peak for the sample compressed at 293K are attributed to the transformation DM →A, indicating that for a certain extent the formation of the TM is also possible during the stress induced MT along [011]. On the basis of data given in Table 3.9, it is possible to give a rough estimate for of the volume fraction of the stabilized, DM, martensite, *x* for the second peak in Figure 3.15a. We can write

$$\frac{q_{h1}}{q_h} = (1 - x_M)\frac{Q_{h1}}{Q_h} \cong 1 - x_M = 0.79, \tag{3.23}$$

where $x_M = \frac{n_2}{n}$ and n is the number of moles of the sample and n_1 and n_2 denotes the numbers of moles of TM and DM, respectively ($n = n_1 + n_2$). Thus, the estimated transformed volume fraction of the stabilized martensite x_M= 0.21 [6].

The shift of the peak temperature in Figure 3.15, i.e. the overheating, is due to the difficulty of re-twinning of DM (or of nucleation of A from DM): once it happens the transformation to austenite can be easy and fast, burst-behavior [19, 56, 60-64]. Thus, the above nucleation barrier is important and one can get an expression for ΔT as follows. Using Eqns (1.16b) and (1.18) from Chapter 1.4, it can be written as:

$$\begin{aligned}
\Delta T = T_p^{DM\to A} - T_P^{TM\to A} &= \frac{A_{fDM} + A_{sDM}}{2} - \frac{A_{fTM} + A_{sTM}}{2} \\
&= \Delta T_o + \frac{d_{1DM} + d_{oDM} + e_{1DM} + e_{oDM}}{-2\Delta s_{DM}} \\
&- \frac{d_{1TM} + d_{oTM} + e_{1M} + e_{oTM}}{-2\Delta s_{TM}} \\
&\cong \frac{2(d_{oDM} - d_{0TM}) + 2e_{oDM} - (e_{1TM} + e_{oTM})}{-2\Delta s} \\
&\cong \frac{\Delta d_n}{-\Delta s} = \frac{\Delta \mathcal{D}}{-\Delta S} = \frac{D_{DM} - D_{TM}}{-\Delta S}.
\end{aligned} \tag{3.24}$$

Here we assumed that $\Delta T_o \cong 0, \Delta s_{DM} \cong \Delta s_{TM}$, $d_{oi} = d_{1i}$ (*i=DM, TM*) and ($e_{1DM} - e_{0DM} \cong 0$ (the branch belonging to the burst like peak is almost vertical: see also Eqn. (1.19)) as well as that the main difference in the first term is due to the difference of the nucleation energy, $(d_{0DM} - d_{oTM}) = \Delta d_n$ (i.e. we use that d_{oi} and d_{1i} contains the sum of the frictional and

nucleation terms, and assume that the frictional type dissipation is the same in both processes). D_{DM} and D_{TM} are the dissipative energies for the heating processes. Now, $\Delta T = 35K$, and using the transformation entropy (1.0 J/molK) for this (A) alloy $\Delta D = 35\,J/mol$. This can be compared with the half of dissipation energy of the of thermally induced transformation (11.8 *J/mol*) i.e. 5.9 *J/mol,* which shows that difference of the nucleation energies of DM and TM is about five time larger than the dissipative energy during the thermally induced heating [6-7]. Thus, the role of the nucleation barrier indeed is important in causing the shift of the peak temperature.

3.2.3.2. Interpretation of AE for complete super-elastic cycles during compression

In addition to Figure 3.11b, Figures 3.19 and 3.20 show the stress-strain curves and its derivatives in comparison with the AE activity and the AE cumulative number [65-66]. From Figures. 3.11, 3.19 and 3.20 the following conclusions can be obtained:

i) In the loading curves: there is a large AE activity in the first (almost linear) part of the $\sigma\sim t\ (\sim\varepsilon)$ curve, which is usually attributed to elastic deformation of the austenite. However, as Figure 3,19a demonstrates the $\frac{d\sigma}{dt}$ curve shows a deviation from the horizontal line at around the same time from which the AE activity increases and it is in accordance with the sharp increase in E_Σ in Figure 3.19b. In addition there is a drop in the AE activity (and a small jump in E_Σ) just at the position of the first stress drop and after it the process remains "silent" (with well decreased AE activity) during the plateau region. Interestingly there is a local maximum of the activity at the second stress drop too (which can be hardly recognizable in Figure 3.19b, but well visible in Fig. 3.19a). The stress drops are related to the nucleation of DM: after the first stress drop the stress is still high enough to maintain the growth of TM until the next nucleation of DM happens. The increase of the activity and the jump in E_Σ at the bending point of the $\sigma\sim t\ (\sim\varepsilon)$ can be attributed to the fact that a slight change in the slope of the $\sigma\sim t\ (\sim\varepsilon)$ curve indicates that the MT starts much earlier than the plateau is reached [67] and this is also accompanied with a detectable AE activity [66].

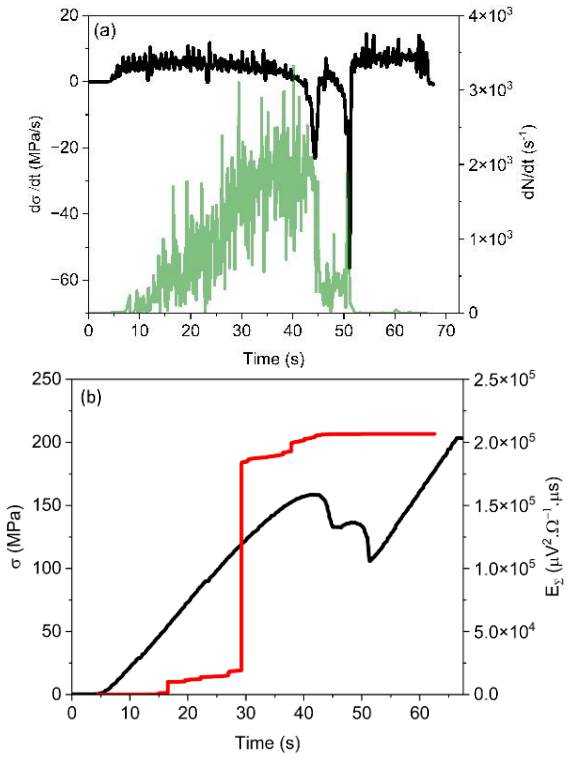

Figure 3.19 the derivative of the stress by time ($\frac{d\sigma}{dt}$) and activity $\frac{dN}{dt}$ versus time, (a) *the stress (σ) and $E_\Sigma$versus time, for loading [6].*

ii) **In the unloading curves:** the small change in the slope of the σ~t *(~ε)* curve and the accompanied small peak at about (85s) presumably belongs to nucleation of small amount TM (and/or partial re-twining of DM) with small jumps in E_Σ as shown in the insert of Fig. 3.20b too). Furthermore all maxima on the derivative of the stress-time curve belong a corresponding local maximum on the AE activity. It can also be seen that there are small kinks at about 100 and 104s on the σ~t curve in Fig. 3.20b, indicating step-like character of the dissolution of DM. The largest change in E_Σ appears at the second stress jump and at this time an audible click was heard.

Finally, since the AE signals are related to sudden local strain- changes [68], the nucleation events in both directions can be sources of AE signals. The sudden stress drops can be related to nucleation/dissolution of detwinned martensite. *This is supported by the fact that the final detwinned martensite,*

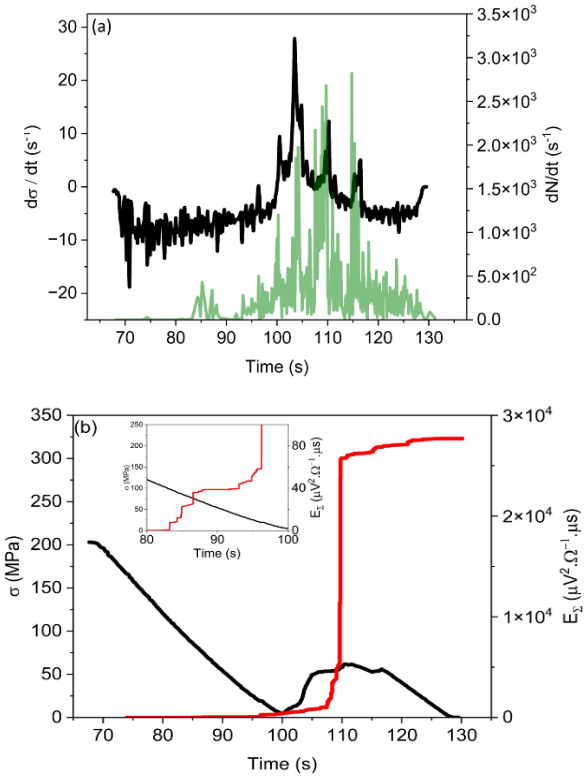

Figure 3.20 the derivative of the stress by time ($\frac{d\sigma}{dt}$) and activity $\frac{dN}{dt}$ versus time, (a) *the stress (σ) and E_Σ versus time, for unloading [6].*

obtained below a certain deformation temperature, was stable even after unloading: during heating it showed a burst like recovery, at about 35K higher transformation temperature than that of the thermally induced one, with an audible click. The observed asymmetry (i.e. the loading process is more noisy than the unloading one) can be related to the fact that the nucleation of the more stable phase (the DM) is more difficult [6, 55,59].

The exponents obtained for the energy and amplitude PDF's for loading/unloading was similar to the exponents for thermally induced MT upon cooling/heating, burst like transition and loading/unloading within the error bars. This latter observation is in accordance with the quite robust behaviour of the characteristic exponents: these are not very sensitive to the details of the source mechanisms of AE events.

Summary

In my thesis, I investigated the thermal and stress-induced MT in $Ni_{49}Fe_{18}Ga_{27}Co_6$ shape memory alloys (SMAs) using acoustic emission analysis. The SCs during MT proceeds by intermittent processes under slowly changing external driving field and has a stop-and-go character. This results in emission of different types of noises including thermal, magnetic, and acoustic emissions. These noises consist of the so-called avalanches; defined as a burst of forward motion of interface quantified as velocity/voltage profile through an interval of time. These avalanches are characterized by their amplitude, duration, size, and energy.

In the first part of my thesis, I investigated the enigma problem of AE and correspondence between the experimental AE results and the mean field theory (MFT) as well as I proposed the introduction of a new scaling parameter φ. I carried out DSC and acoustic investigations on a special setup that was utilized at the university of Debrecen for simultaneous measurement of DSC and AE by our group. 10K/min scanning rate of the driving parameter was used in my measurements. The most important statements of this part:

1.1. I show that in the theoretically predicted temporal shape of acoustic emission avalanches averaged at fixed area

$$V_{av}(t) = \mathrm{at}e^{-(\frac{t}{\tau_s})^{\delta}} \tag{S1}$$

(τ_s and a non-universal, material-dependent constants, δ=2 in MFT), the maximum amplitude A_m is proportional to t_m (the rising time, $t_m \sim \tau_s$) and they are interrelated assuming a power relation, $\frac{A_m}{t_m}(\sim a) \sim A_m^{\varphi}$, i.e.

$$t_m \sim A_m^{1-\varphi}. \tag{S2}$$

The above conjecture is supported by the self-similarity of crackling noises, which suggests a power relation between different parameters [4].

1.2. The validity of (S2) is demonstrated by my experimental results obtained from acoustic emission for thermally induced martensitic transformation in $Ni_{49}Fe_{18}Ga_{27}Co_6$ shape memory single crystal during heating and $\varphi = 0.6$ is

obtained. The same analysis provided same value for φ from data measured earlier by N. Samy et al. in my group on $Ni_{45}Co_5Mn_{36.6}In_{13.4}$ single crystal [4].

1.3. On the basis of (S2), I also show that the well-known scaling relations between the area and A_m as well as between A_m and the energy of acoustic emission signals have the form

$$S \sim A_m^{2-\varphi} \tag{S3}$$

and

$$E \sim A_m^{3-\varphi}. \tag{S4}$$

(S3) and (S4) give back the power exponents predicted by the mean field theory (and assuming no distortion of the measured parameters by signal transfer problems) only if $\varphi = 0$, while the "enigma of acoustic emission" known in the literature is obtained with $\varphi = 1$ [S1]. Exponents obtained from relations (S3) and (S4) are in reasonable agreement with each other and with φ values obtained from (S2) and provided an average value $\varphi \cong 0.74 \pm 0.13$ [4].

1.4. Using the average value of φ the voltage and the time scales of the $V(t)$ function were normalized by A_m and $A_m^{1-\varphi}$, and the obtained averaged curves for different constant values of area, S, collapsed nicely on each other providing good universal behaviour [4].

I devoted the second part to AE study of the anomalous stress-strain curves produced by compression along [011] orientation. The anomaly is defined by the overall negative plateau in addition to the presence of local stress drops during loading, A$\rightarrow M$. Interestingly, depending on the test temperature. I observed two unloading regimes, M$\rightarrow A$. Above a certain temperature superelastic behavior with local jumps on the stress-strain curve, on both loading and unloading branches, was obtained, while below it the sample remained in martensite after unloading and showed a burst like transition to austenite. I did my experiment using a special setup that is utilized at the University of Debrecen, during my PhD, for simultaneous measurement of stress-strain curves and AE. The results can be summarized as follows:

2.1. For loading the gradually increased AE activity well below the maximum on the σ versus t function can be attributed to the nucleation of the twinned martensite. The two stress drops are attributed to the subsequent nucleation of the detwinned (more stable) martensite from the twinned martensite [6,7].

2.2. The sharp decrease of the AE activity just at the stress drops indicates that the formation of the detwinned modification is a sudden, fast process and can take place without significant elastic energy storage. This is supported by the fact that during burst like thermal recovery the width of the transition is very small [6].

2.3. The final detwinned martensite, obtained below a certain deformation temperature, is stable even after uploading: during heating it showed a burst-like recovery, at about 35K higher transformation temperature than that of the thermally induced one, with an audible click [6].

2.4. For unloading the first part shows a moderate deviation of the stress versus time curve from the linear (elastic) regime and the observed acoustic activity in this region presumably belongs to nucleation of small amount of the twinned martensite (i.e. to partial retwinning). At all stress jumps there are local maxima on the AE activity curve. These are interpreted by sudden dissolution of the detwinned phase (retwinning) [6,7].

Összefoglalás

Disszertációmban termikus- és feszültség-indukált martenzites transzformációt, MT, vizsgáltam akusztikus emissziós (AE) analízis segítségével $Ni_{49}Fe_{18}Ga_{27}Co_5$ alakemlékező ötvözetekben (AEÖ). Gyengén változó külső terekben lejátszódó MT során a szerkezet-változások szakaszos folyamatok révén valósulnak meg és megáll-újraindul jellegűek. Ez különböző típusú (termikus, mágneses és akusztikus) zajok emissziójához vezet. Ezek a zajok un. lavinákból állnak, amelyeket a mozgó határfelületek robbanás-szerű elmozdulása vált ki, és időben változó sebesség/feszültség profilokkal tartoznak hozzájuk. A lavinákat azok amplitúdója, időtartama, mérete és energiája jellemzik.

Disszertációm első részben az AE enigma problémát, valamint a kísérleti AE eredmények és az átlagtér elmélet közötti egyezést vizsgáltam valamint javasoltam egy új, φ, skálaparaméter bevezetését. A DSC és akusztikus emissziós vizsgálatokat a Debreceni Egyetemen csoportunkban a DSC és AE szimultán vizsgálatára kifejlesztett mérési elrendezésben végeztem. A vezérlő paraméter 10K/min-es pásztázó sebességét alkalmaztam valamennyi mérésemnél. Ennek a résznek a legfontosabb eredményei:

1.1. Megmutattam, hogy az akusztikus emissziós lavinák rögzített terület mellett átlagolt időalakjára elméletileg jósolt időfüggvényben

$$V(t) = ate^{-\left(\frac{t}{\tau_s}\right)^{\delta}} \tag{S1}$$

(τ_s és a nem unverzális, anyagfüggő konstansok, $\delta=2$ az átlagtér elméletben), a maximális amplitúdó, A_m, arányos t_m-el (az emelkedési idővel, $t_m \sim \tau_s$) és ezeket egy hatványfüggvény kapcsolja össze, $\frac{A_m}{t_m}(\sim a) \sim A_m^{\varphi}$, azaz

$$t_m \sim A_m^{1-\varphi}. \tag{S2}$$

A fenti feltételezést a recsegő zajok ön-hasonlósága támasztja alá, amely azt sugallja, hogy a különböző paraméterek között hatvány-függvény összefüggés van [4].

1.2. (S2) érvényességét $Ni_{49}Fe_{18}Ga_{27}Co_6$ alakemlékező egykristályon általam fűtés közben mért termikusan indukált martenzites átalakulás során kapott akusztikus emisszióból kapott kísérleti eredményekkel illusztráltam és $\varphi = 0.6$ adódott. Ugyan ilyen analízis ugyanezt az eredmény szolgáltatták φ-re N. Samy és mts. által csoportunkban $Ni_{45}Co_5Mn_{36.6}In_{13.4}$ egykristályon mért adatai is [4].

1.3. (S2) alapján azt is megmutattam, hogy a jól ismert skála összefüggések az akusztikus emissziós jelek területe, S, és amplitúdója, A_m, valamint energiája, E és amplitúdója között a következő alakúak

$$S \sim A_m^{2-\varphi} \tag{S3}$$

és

$$E \sim A_m^{3-\varphi}. \tag{S4}$$

(S3) és (S4) az átlag tér elmélet szerint jósolt exponenseket (feltételezve azt is, hogy a jelátviteli problémák nem okoznak torzításokat) csak akkor adják vissza, ha $\varphi = 0$, míg az irodalomban jól ismert akusztikus emissziós rejtély ("enigma of acoustic emission") $\varphi=1$ esetén adódik [S1]. Az (S3) és (S4) összefüggések alapján kapott exponensek jó egyezéseben voltak egymással és az (S2) alapján kapott φ értékekkel és $\varphi \cong 0.74 \pm 0.13$ átlagértéket szolgáltatták [4].

1.4. Felhasználva φ átlagértékét az V(t) függvények feszültség és idő skáláit A_m-el valamint $A_m^{1-\varphi}$-el skálázva, a különböző konstans S értékekhez tartozó átlagolt görbék jól egymásra estek jó univerzális viselkedést tükrözve. [4].

Disszertációm második részét a $[011]_A$ irány mentén összenyomás során kapott anomális feszültség-deformáció hurkok AE-os vizsgálatának szenteltem. Az anomáliát az átlagos negatív plató, valamint terhelés során ($A \rightarrow M$), lokális feszültség esések jelentléte jellemzik. Érdekes módon, a vizsgálati hőmérséklettől függően, két visszaterhelési ($M \rightarrow A$) viselkedést figyeltem meg. Bizonyos hőmérséklet fölött szuperelasztikus feszültség-deformáció hurkokat kaptam, melyek feszültség-ugrásokat tartalmaztak, míg

ez alatt a minta mertenzites állapotban maradt és ugrás-szerűen tért vissza ausztenitbe felmelegítés során. Speciális, a Debreceni Egyetemen, doktori vizsgálataim során, kifejlesztett mérési elrendezést alkalmaztam az AE és a feszültség-deformációs görbék szimultán vizsgálatára. Az eredményeket a következőkben lehet összefoglalni:

2.1. A σ(t) függvényen, terheléskor jóval a feszültség maximum alatt megfigyelt, fokozatosan növekvő AE aktivitást az ikresedett martenzit nukleációjával lehetett azonosítani. A két feszültség esés a (stabilabb) iker-mentes martenzitnek az ikresedett martenzitből történő, egymást követő, nukleációjánk tulajdonítható [6,7].

2.2. A feszültségek esések utáni éles AE aktivitás csökkenés azt jelzi, hogy az iker-mentes matrenzit módosulat képződése egy hirtelen, gyors folyamat és jelentős rugalmas energia tárolás nélkül történik. Ezt az a tény is megerősíti, hogy az ugrás-szerű termikus megújulás során az átmenet szélessége nagyon kicsi [6].

2.3. A bizonyos deformációs hőmérséklet alatt kapott iker-mentes martenzit stabil maradt a feszültség elvétele után is: melegítés során ugrás-szerű, hallható kattanással járó, vissza-transzformációt mutatott 35 K-el magasabb hőmérsékletnél, mint ami a termikusan indukált átalakuláshoz tartozik [6].

2.4. A terhelés csökkentése során a feszültség-idő függvényen moderált eltérések voltak láthatók az eredetileg lineáris (rugalmas) viselkedéstől és a megfigyelt akusztikus aktivitás ebben tartományban az ikresedett matenzit kis mennyiségű nukleációjának (azaz részleges újra-ikresedésnek) tulajdonítható. Valamennyi feszültség ugrásnál lokális maximumok vannak az AE aktivitás görbéken. Ezeket az ikermentes martenzit hirtelen feloldódásával (újra-ikresedéssel) magyaráztuk [6,7].

2.5. Az AE lavinák paraméterei minden esetben a szokásos (hatvány függvény) viselkedést mutatták és például az energia kitevők hibahatáron belül megegyeztek a termikus, illetve feszültség indukál transzformációkra mindkét irányban [6].

Bibliography

[1] Sethna, J. P., Dahmen, K. A., & Myers, C. R. (2001). Crackling noise. Nature, 410(6825), 242-250. https://doi.org/10.1038/35065675

[2] Beke, D. L., Daróczi, L., Tóth, L. Z., Bolgár, M. K., Samy, N. M., & Hudák, A. (2019). Acoustic emissions during structural changes in shape memory alloys. Metals, 9(1), 58. https://doi.org/10.3390/met9010058

[3] Casals, B., Dahmen, K. A., Gou, B., Rooke, S., & Salje, E. K. (2021). The duration-energy-size enigma for acoustic emission. Scientific reports, 11(1), 5590. https://doi.org/10.1038/s41598-021-84688-7

[4] Kamel, S. M., Samy, N. M., Tóth, L. Z., Daróczi, L., & Beke, D. L. (2022). Denouement of the energy-amplitude and size-amplitude enigma for acoustic-emission investigations of materials. Materials, 15(13), 4556. https://doi.org/10.3390/ma15134556

[5] Bolgár, M. K., Daróczi, L., Tóth, L. Z., Timofeeva, E. E., Panchenko, E. Y., Chumlyakov, Y. I., & Beke, D. L. (2017). Effect of γ precipitates on thermal and acoustic noises emitted during austenite/martensite transformation in NiFeGaCo single crystals. Journal of Alloys and Compounds, 705, 840-848. https://doi.org/10.1016/j.jallcom.2017.02.167

[6] Kamel, S. M., Daróczi, L., Tóth, L. Z., Panchenko, E., Chumljakov, Y. I., Samy, N. M., & Beke, D. L. (2023). Acoustic emission and DSC investigations of anomalous stress-stain curves and burst like shape recovery of Ni49Fe18Ga27Co6 shape memory single crystals. Intermetallics, 159, 107932. https://doi.org/10.1016/j.intermet.2023.107932

[7] Beke, D. L., Kamel, S. M., Daróczi, L., & Tóth, L. Z. (2022). Thermodynamic Analysis of Anomalous Shape of Stress–Strain Curves for Shape Memory Alloys. Materials, 15(24), 9010. https://doi.org/10.3390/ma15249010

[8] Otsuka, K., & Ren, X. (1999). Recent developments in the research of shape memory alloys. Intermetallics, 7(5), 511-528. https://doi.org/10.1016/S0966-9795(98)00070-3

[9] Naresh, C., Bose, P. S. C., & Rao, C. S. P. (2016, September). Shape memory alloys: a state of art review. In IOP conference series: materials science and engineering (Vol. 149, No. 1, p. 012054). IOP Publishing. https://doi.org/10.1088/1757-899X/149/1/012054

[10] Jani, J. M., Leary, M., Subic, A., & Gibson, M. A. (2014). A review of shape memory alloy research, applications and opportunities. Materials & Design (1980-2015), 56, 1078-1113. https://doi.org/10.1016/j.matdes.2013.11.084

[11] Lagoudas, D. C. (Ed.). (2008). Shape memory alloys: modeling and engineering applications. Springer Science & Business Media. https://doi.org/10.1007/978-0-387-47685-8

[12] Darjan, C., & Dolinsek, J. (2007). Shape memory alloys. Univerza v Ljubljani, Fakulteta za Matemetiko in Fiziko, Odelek za Fiziko.

[13] Al-Humairi, S. N. S. (2020). Cu-based shape memory alloys: modified structures and their related properties. Recent advancements in the metallurgical engineering and electrodeposition, 25.

[14] Tsuchiya, K. (2011). Mechanisms and properties of shape memory effect and superelasticity in alloys and other materials: A practical guide. In Shape Memory and Superelastic Alloys (pp. 3-14). Woodhead Publishing. https://doi.org/10.1533/9780857092625.1.3

[15] Guo, Y., Klink, A., Fu, C., & Snyder, J. (2013). Machinability and surface integrity of Nitinol shape memory alloy. CIRP Annals, 62(1), 83-86. https://doi.org/10.1016/j.cirp.2013.03.004

[16] Panchenko, E., Timofeeva, Panchenko, E., Timofeeva, Eftifeeva, A., Osipovich, K., Surikov, N., Chumlyakov, Y., Gerstein, G., & Maier, H. J. (2019). Giant rubber-like behavior induced by martensite aging in Ni51Fe18Ga27Co4 single crystals. Scripta Materialia, 162, 387-390. https://doi.org/10.1016/j.scriptamat.2018.12.003

[17] Panchenko, E., Timofeeva, E., Chumlyakov, Y., Osipovich, K., Tagiltsev, A., Gerstein, G., & Maier, H. J. (2019). Compressive shape memory actuation

response of stress-induced martensite aged Ni51Fe18Ga27Co4 single crystals. Materials Science and Engineering: A, 746, 448-455. https://doi.org/10.1016/j.msea.2019.01.004.

[18] Beke, D. L., Daróczi, L., Samy, N. M., Tóth, L. Z., & Bolgár, M. K. (2020). On the thermodynamic analysis of martensite stabilization treatments. Acta Materialia, 200, 490-501. https://doi.org/10.1016/j.actamat.2020.09.026

[19] Machlin, E. S., & Cohen, M. (1951). Burst phenomenon in the martensitic transformation. JOM, 3, 746-754. https://doi.org/10.1007/BF03397387

[20] Nikolaev, V. I., Stepanov, S. I., Yakushev, P. N., Krymov, V. M., & Kustov, S. B. (2020). Burst-like shape recovery and caloric effects in Ni–Fe–Ga–Co single crystalline shape memory alloys. Intermetallics, 119, 106709. https://doi.org/10.1016/j.intermet.2020.106709

[21] Beke, D. L., Daróczi, L., & Elrasasi, T. Y. (2013). Determination of elastic and dissipative energy contributions to martensitic phase transformation in shape memory alloys. Shape Memory Alloys-Processing, Characterization and Applications; Fernandes, F., Ed, 167. https://dx.doi.org/10.5772/51511

[22] Beke, D. L., Bolgár, M. K., Tóth, L. Z., & Daróczi, L. (2018). On the asymmetry of the forward and reverse martensitic transformations in shape memory alloys. Journal of Alloys and Compounds, 741, 106-115. https://doi.org/10.1016/j.jallcom.2017.11.271

[23] Salje, E. K., & Dahmen, K. A. (2014). Crackling noise in disordered materials. Annu. Rev. Condens. Matter Phys., 5(1), 233-254. https://doi.org/10.1146/annurev-conmatphys-031113-133838

[24] Carrillo, L., & Ortín, J. (1997). Avalanches in the growth of stress-induced martensites. Physical Review B, 56(18), 11508. https://doi.org/10.1103/PhysRevB.56.11508

[25] Salje, E. K., Planes, A., & Vives, E. (2017). Analysis of crackling noise using the maximum-likelihood method: Power-law mixing and exponential

damping. Physical Review E, 96(4), 042122. https://doi.org/10.1103/PhysRevE.96.042122

[26] Tóth, L. Z., Daróczi, L., Szabó, S., & Beke, D. L. (2016). Simultaneous investigation of thermal, acoustic, and magnetic emission during martensitic transformation in single-crystalline Ni 2 MnGa. Physical Review B, 93(14), 144108. https://doi.org/10.1103/PhysRevB.93.144108

[27] Bükki-Deme, A. Impulzus alapú Barkhausen-zaj vizsgálat szerkezeti acélokon. PhD Theses, University of Debrecen. 2011. http://hdl.handle.net/2437/104531

[28] Wiese, K. J. (2022). Theory and experiments for disordered elastic manifolds, depinning, avalanches, and sandpiles. Reports on Progress in Physics, 85(8), 086502. https://doi.org/10.1088/1361-6633/ac4648

[29] Kuntz, M. C., & Sethna, J. P. (2000). Noise in disordered systems: The power spectrum and dynamic exponents in avalanche models. Physical Review B, 62(17), 11699. https://doi.org/10.1103/PhysRevB.62.11699

[30] Ràfols, I., & Vives, E. (1995). Statistics of avalanches in martensitic transformations. II. Modeling. Physical Review B, 52(17), 12651. https://doi.org/10.1103/PhysRevB.52.12651

[31] Planes, A., Mañosa, L., & Vives, E. (2013). Acoustic emission in martensitic transformations. Journal of Alloys and Compounds, 577, S699-S704. https://doi.org/10.1016/j.jallcom.2011.10.082

[32] LeBlanc, M., Angheluta, L., Dahmen, K., & Goldenfeld, N. (2013). Universal fluctuations and extreme statistics of avalanches near the depinning transition. Physical Review E, 87(2), 022126. https://doi.org/10.1103/PhysRevE.87.022126

[33] Durin, G., & Zapperi, S. (2000). Scaling exponents for Barkhausen avalanches in polycrystalline and amorphous ferromagnets. Physical review letters, 84(20), 4705. https://doi.org/10.1103/PhysRevLett.84.4705

[34] Papanikolaou, S., Bohn, F., Sommer, R. L., Durin, G., Zapperi, S., & Sethna, J. P. (2011). Universality beyond power laws and the average avalanche shape. Nature Physics, 7(4), 316-320. https://doi.org/10.1038/nphys1884

[35] Laurson, L., Illa, X., Santucci, S., Tore Tallakstad, K., Måløy, K. J., & Alava, M. J. (2013). Evolution of the average avalanche shape with the universality class. Nature communications, 4(1), 2927. https://doi.org/10.1038/ncomms3927

[36] Dobrinevski, A., Le Doussal, P., & Wiese, K. J. (2015). Avalanche shape and exponents beyond mean-field theory. Europhysics Letters, 108(6), 66002. https://doi.org/10.1209/0295-5075/108/66002

[37] Panchenko, E. Y., Timofeeva, E. E., Kazantseva, L. P., Chumlyakov, Y. I., & Maier, H. (2011). The effect of heat treatment on mechanisms of martensitic transformations in ferromagnetic [Ni. sub. 49][Fe. sub. 18][Ga. sub. 27][Co. sub. 6] single crystals. Russian Physics Journal, 53(11), 1219-1223. https://doi.org/10.1007/s11182-011-9552-0

[38] Chumlyakov, Y. I., Kireeva, I. V., Panchenko, E. Y., Kirillov, V. A., Timofeeva, E. E., Kretinina, I. V., Danilson, Y. N., Karaman, I., Maier, H., & Cesari, E. (2012). Thermoelastic martensitic transformations in single crystals with disperse particles. Russian Physics Journal, 54, 937-950. https://doi.org/10.1007/s11182-011-9701-5

[39] Timofeeva, E. E., Panchenko, E. Yu, Chumlyakov, Y. I., Vetoshkina, N. G. and H. J. Maier. (2015) "One-way and two-way shape memory effect in ferromagnetic NiFeGaCo single crystals." Materials Science and Engineering: A 640, 465-470. https://doi.org/10.1016/j.msea.2015.06.024

[40] Höhne, G. W. H., Hemminger, W. F., Flammersheim, H. J., Höhne, G. W. H., Hemminger, W. F., & Flammersheim, H. J. (2003). Differential Scanning Calorimetry, 122-152.

[41] Ortin, J., & Planes, A. (1988). Thermodynamic analysis of thermal measurements in thermoelastic martensitic transformations. Acta metallurgica, 36(8),1873-1889. https://doi.org/10.1016/00016160(88)90291-X

[42] Mohareb, N. S. S. (2021). Investigation of Noisy Character of Phase Transformations in Ferromagnetic Shape Memory Materials. Debrecen Egyetem

[43] Tóth, L. Z. (2018). Fázisátalakulást kísérő zajok vizsgálata Ni2MnGa alakemlékező ötvözetekben. Debrecen Egyetem.

[44] White, E. P., Enquist, B. J., & Green, J. L. (2008). On estimating the exponent of power-law frequency distributions. Ecology, 89(4), 905-912. https://doi.org/10.1890/07-1288.1

[45] Clauset, A., Shalizi, C. R., & Newman, M. E. (2009). Power-law distributions in empirical data. SIAM review, 51(4), 661-703. https://doi.org/10.1137/070710111

[46] Bolgár, M. K., L. Z. Tóth, S. Szabó, Sz Gyöngyösi, L. Daróczi, E. Y. Panchenko, Y. I. Chumlyakov, and D. L. Beke. (2016). Thermal and acoustic noises generated by austenite/martensite transformation in NiFeGaCo single crystals. Journal of Alloys and Compounds, 658, 29-35. https://doi.org/10.1016/j.jallcom.2015.10.173

[47] Tóth, L. Z., Szabó, S., Daróczi, L., & Beke, D. L. (2014). Calorimetric and acoustic emission study of martensitic transformation in single-crystalline Ni 2 MnGa alloys. Physical Review B, 90(22), 224103. https://doi.org/10.1103/PhysRevB.90.224103

[48] Chi-Cong, V., & Weiss, J. (2020). Asymmetric damage avalanche shape in quasibrittle materials and subavalanche (aftershock) clusters. Physical Review Letters, 125(10), 105502. https://doi.org/10.1103/PhysRevLett.125.105502

[49] Sparks, G., & Maass, R. (2018). Shapes and velocity relaxation of dislocation avalanches in Au and Nb microcrystals. Acta Materialia, 152, 86-95. https://doi.org/10.1016/j.actamat.2018.04.007

[50] Antonaglia, J., Wright, W. J., Gu, X., Byer, R. R., Hufnagel, T. C., LeBlanc, M., Uhl, J. T., & Dahmen, K. A. (2014). Bulk metallic glasses deform via slip avalanches. Physical review letters, 112(15), 155501. https://doi.org/10.1103/PhysRevLett.112.155501

[51] Samy, N. M., Bolgár, M. K., Barta, N., Daróczi, L., Tóth, L. Z., Chumlyakov, Y. I., Karaman, I., & Beke, D. L. (2019). Thermal, acoustic and magnetic noises emitted during martensitic transformation in single crystalline Ni45Co5Mn36. 6In13. 4 meta-magnetic shape memory alloy. Journal of Alloys and Compounds, 778, 669-680. https://doi.org/10.1016/j.jallcom.2018.11.149

[52] Baro, J. (2018). Avalanches in Out of Equilibrium Systems: Statistical Analysis of Experiments and Simulations (Doctoral dissertation, University of Barcelona).

[53] Vives, E., Baró, J., & Planes, A. (2016). From labquakes in porous materials to earthquakes. In Avalanches in Functional Materials and Geophysics (pp. 31-58). Cham: Springer International Publishing. https://doi.org/10.1007/978-3-319-45612-6_3

[54] Nikolaev, V. I., Yakushev, P. N., Malygin, G. A., Averkin, A. I., Pulnev, S. A., Zograf, G. P., Kustov, S. B., & Chumlyakov, Y. I. (2016). Influence of partial shape memory deformation on the burst character of its recovery in heated Ni–Fe–Ga–Co alloy crystals. Technical Physics Letters, 42, 399-402. https://doi.org/10.1134/S1063785016040209

[55] Nikolaev, V. I., Yakushev, P. N., Malygin, G. A., & Pul'nev, S. A. (2010). Burst character of thermoelastic shape memory deformation in ferromagnetic Ni-Fe-Ga-Co alloy. Technical Physics Letters, 36, 914-917. https://doi.org/10.1134/S1063785010100123

[56] Tóth, L. Z., Daróczi, L., Panchenko, E., Chumlyakov, Y., & Beke, D. L. (2020). Acoustic emission characteristics and change the transformation entropy after stress-induced martensite stabilization in shape memory Ni53Mn25Ga22 single crystal. Materials, 13(9), 2174. https://doi.org/10.3390/ma13092174

[57] Chandrasekaran, M., Cooreman, L., Van Humbeeck, J., & Delaey, L. (1989). Martensitic transformation in Cu Zn Al: Changes in transformation entropy due to post quench ageing in the β or martensitic condition. Scripta metallurgica, 23(2), 237-239. https://doi.org/10.1016/0036-9748(89)90418-3

[58] Ren, X., Miura, N., Zhang, J., Otsuka, K., Tanaka, K., Koiwa, M., Suzuki, T., Chumlyakov, Y. I., & Asai, M. (2001). A comparative study of elastic constants of Ti–Ni-based alloys prior to martensitic transformation. Materials Science and Engineering: A, 312(1-2),196-206. https://doi.org/10.1016/S0921-5093(00)01876-1

[59] Lázpita, P., Villa, E., Villa, F., & Chernenko, V. (2021). Temperature Dependent Stress–Strain Behavior and Martensite Stabilization in Magnetic Shape Memory Ni51. 1Fe16. 4Ga26. 3Co6. 2 Single Crystal. Metals, 11(6), 920. https://doi.org/10.3390/met11060920

[60] Malygin, G. A., Nikolaev, V. I., Krymov, V. M., Pul'nev, S. A., & Stepanov, S. I. (2019). Interfacial Stresses and Anomalous Shape of Pseudoelastic Deformation Curves in Ni 49 Fe 18 Ga 27 Co 6 Alloy Crystals Compressed along the [011] A Axis. Technical Physics, 64, 819-827. https://doi.org/10.1134/S1063784219060124

[61] L'vov, V. A., Rudenko, A. A., Chernenko, V. A., Cesari, E., Pons, J., & Kanomata, T. (2005). Stress-induced martensitic transformation and superelasticity of alloys: Experiment and theory. Materials transactions, 46(4), 790-797. https://doi.org/10.2320/matertrans.46.790

[62] Picornell, C., Pons, J., & Cesari, E. (2004). Stress–temperature relationship in Cu–Al–Ni single crystals in compression mode. Materials Science and Engineering: A, 378(1-2), 222-226. https://doi.org/10.1016/j.msea.2003.10.347

[63] Samy, N. M., Daróczi, L., Tóth, L. Z., Panchenko, E., Chumlyakov, Y., Surikov, N., & Beke, D. L. (2020). Effect of stress-induced martensite stabilization on acoustic emission characteristics and the entropy of martensitic transformation in shape memory Ni51Fe18Ga27Co4 single crystal. Metals, 10(4), 534. https://doi.org/10.3390/met10040534

[64] Picornell, C., Pons, J., & Cesari, E. (2001). Stabilisation of martensite by applying compressive stress in Cu-Al-Ni single crystals. Acta materialia, 49(20),4221-423. **https://doi.org/10.1016/S1359-6454(01)00308-1**

[65] Weidner, A., Vinogradov, A., Vollmer, M., Krooß, P., Kriegel, M. J., Klemm, V., Chumljakov, Y., Niendorf, T., & Biermann, H. (2021). In situ characterization of the functional degradation of a [001] orientated Fe–Mn–Al–Ni single crystal under compression using acoustic emission measurements. Acta Materialia, 220, 117333. **https://doi.org/10.1016/j.actamat.2021.117333**

[66] Landa, M. I. C. H. A. L., Novák, V., Blahácek, M., & Šittner, P. (2002). Transformation processes in shape memory alloys based on monitoring acoustic emission activity. J. Acoust. Emission, 20, 163-171.

[67] Zoubková, K., Seiner, H., Sedlák, P., Villa, E., Tahara, M., Hosoda, H., & Chernenko, V. (2022). Non-linear elastic behavior of Ni-Fe-Ga (Co) shape memory alloy and Landau-energy landscape reconstruction. Acta Materialia, 224, 117530. **https://doi.org/10.1016/j.actamat.2021.117530**

[68] Wollants, P., Roos, J. R., & Delaey, L. (1993). Thermally-and stress-induced thermoelastic martensitic transformations in the reference frame of equilibrium thermodynamics. Progress in Materials Science, 37(3), 227-288. **https://doi.org/10.1016/0079-6425(93)90005-6**

Appindex I

For scaling relations containing the energy we can start from from the definition of E and use Eqn. (3.15), i.e.

$$E \sim V_m^2 t_m \int_o^{T^*} t^{*2} exp(-t^{*2}) dt^* = V_m^2 t_m I. \tag{I.1}$$

The *I* integral has the form:

$$\int_0^{T^*} t^{*2} exp(-t^{*2}) dt^* = \left[-\frac{1}{2} t^* exp(-t^{*2}) + \frac{\sqrt{\pi}}{4} erf t^* \right]_0^{T^*}, \tag{I.2}$$

i.e.

$$I = -\frac{1}{2} T^* \exp\left[-(T^*)^2\right] + \frac{\sqrt{\pi}}{4} erf(T^*) = -\frac{1}{2} \left(\sqrt{2ln \frac{V_m}{C}} \right) \left(\frac{C}{V_m} \right)^2 + \frac{\sqrt{\pi}}{4} erf \sqrt{2ln \frac{V_m}{C}}. \tag{I.3}$$

It can be seen that the value of *I* is always positive (*T*> t_m, i.e. $T^* > 0$). Indeed, for $T^* > 2$ we can take into account that erf 2 ≅ 1 and the first term can be neglected as compared to $\frac{\sqrt{\pi}}{4}$ ($T^* exp(-T^{*2}) = 0.037$ for $T^* = 2$). Thus, $T^* > 2$ also means that in $\frac{\sqrt{\pi}}{4} \left(1 - \frac{2}{\sqrt{\pi}} T^* exp(-T^{*2}) \right)$ the second term is less than 0.05, and we get $I \cong const = \frac{\sqrt{\pi}}{4}$. The $T^* > 2$ requirement leads also to the condition that $\frac{V_m}{C} > 8$. Thus, we have

$$E \sim {V_m}^2 t_m I = \frac{V_m^3 I}{B} = B^2 t_m^3 I \cong B^2 T^3 I \left(2ln \frac{V_m}{C} \right)^{-\frac{3}{2}}, \tag{I.4}$$

and thus

$$\frac{\partial ln E}{\partial ln V_m} = \frac{\partial ln E_{AE}}{\partial ln A_m} \sim 3 - \varphi \tag{I.5}$$

List of Publications

1- Publication related to the dissertation

P1. Kamel, S. M., Samy, N. M., Tóth, L. Z., Daróczi, L., & Beke, D. L. (2022). Denouement of the energy-amplitude and size-amplitude enigma for acoustic-emission investigations of materials. Materials, 15(13), 4556. **https://doi.org/10.3390/ma15134556**

P2. Beke, D. L., Kamel, S. M., Daróczi, L., & Tóth, L. Z. (2022). Thermodynamic Analysis of Anomalous Shape of Stress–Strain Curves for Shape Memory Alloys. Materials, 15(24), 9010. **https://doi.org/10.3390/ma15249010**

P3. Kamel, S. M., Daróczi, L., Tóth, L. Z., Panchenko, E., Chumljakov, Y. I., Samy, N. M., & Beke, D. L. (2023). Acoustic emission and DSC investigations of anomalous stress-stain curves and burst like shape recovery of Ni49Fe18Ga27Co6 shape memory single crystals. Intermetallics, 159, 107932. **https://doi.org/10.1016/j.intermet.2023.107932**

2- Other publications

P4. Daróczi, L., Kamel, S. M., Tahara, M., Chernenko, V., Hosoda, H., Tóth, L. Z., & Beke, D. L. (2024). Acoustic emission during approaching the critical point on stress-temperature diagram of martensitic transformation in Ni48Fe20Co5Ga27 (at.%) single crystal. Intermetallics, 173, 108432. **https://doi.org/10.1016/j.intermet.2024.108432**

P5. Kamel, S.M., Daróczi, L., Tóth, L.Z., Beke, D.L., Juárez, G.G., Cobo, S., Salmon, L., Molnár, G. and Bousseksou, A. (2024). Acoustic emissions from spin crossover complexes. Journal of Materials Chemistry C, 12(16), 5757-5765. **https://doi.org/10.1039/d4tc00495g**

P6. Medhat, M., El-Zaiat, S.Y., Omar, M.F., Farag, S.S. and Kamel, S.M. (2017). Refraction and dispersion measurement using dispersive Michelson interferometer. Optics Communications, 393, 275-283. **https://doi.org/10.1016/j.optcom.2017.02.039**

3 - Conferences

Presentations

C1. Kamel S.M., Daróczi L., Tóth L.Z., Panchenko E., Chumljakov Y.I., N.M. Samy, Beke D.L. Acoustic emission during anomalous stress strain curve along [011] in $Ni_{49}Fe_{18}Ga_{27}Co_6$ shape memory single crystal. Proceedings of the 13th European Symposium on Martensitic Transformations; Lecco, Italy. 26-30 August 2024.

C2. Sarah M Kamel, Lajos Daróczi, László Z. Tóth, Elena Panchenko, Yuriy I. Chumljakov, Dezső L Beke Anomalous Stress-Strain Curve of $Ni_{49}Fe_{18}Ga_{27}Co_6$ Shape Memory Single Crystal: Burst like recovery during heating,15-min talk, DoffI_2021.September 16-18 (meeting of PhD students).

Posters

C3. Kamel S.M., Daróczi L., Tóth L.Z., Panchenko E., Chumljakov Y.I., Beke D.L. Burst like recovery of $Ni_{49}Fe_{18}Ga_{27}Co_6$ shape memory single crystal after compressive stress-strain loading. In: Kockar B., Gortan M.O., editors. Proceedings of the 12th European Symposium on Martensitic Transformations; Ankara, Turkey. 5–9 September 2022; Ankara, Turkey: Hacettepe University; pp. 88–89.

Acknowledgments

Praise to Allah the lord of the worlds

I would like to express my profound gratitude to my advisor ***Prof. Dr. Dezső L. Beke****, who always supported me and put a great effort in guiding me through my PhD work. He introduced me to different research areas in material science. I gained extensive knowledge from his lectures, debats and disscusions on theoritical and experimental results, collaborative paper writing, and my dissertation crafting. He provided me with opportunities to engage with a diverse network of scientific collaboration. It has been an extraordinary scientific journey under his expert guidence and supervision.*

My sincere thanks to ***Prof. Lajos Daróczi****, who provided me with continous help and experimental training. I gained alot of knowledge from his experties. I acquired many skills in handling different laboratory experiments, constructing new setups and find new experimental solutions. I learned alot from his feedbacks and encouragement which enriched my understanding and the quality of my work.*

I express great gratitude to my colleagues for their helpful support. Thanks to ***Dr/ László Z. Tóth*** *for sharing his statistical evaluation program and for providing assistance throughout the data analysis process. Thanks to* ***Nora Samy*** *for her collaboration in preforming DSC measurements and using statistical evaluation program. On personal level she provided me with great assist during my first PhD year.*

I express my extreme gratitude to our collaborative partners ***Prof. Elena Panchenko*** *and* ***Prof. Yuriy I. Chumljakov*** *from Tomsk State University, Russia, for providing the ferromagnetic-shape memory single crystals.*

I express my thanks to ***Prof. Ferenc Kun*** *the head of the doctrol school and* ***Prof. Zoltán Erdélyi*** *the head of the departement of solid-state physics.*

Thanks to the doctrol school of physics and to the Doctoral council. Thanks to ***Dr/ László Olah*** *and* ***Bessenyei Éva*** *for there continuous guidance and assist. Thanks for* ***Dr/ Dorottya Sohler*** *for her patient and aboslut help for checking and finalizing my thesis.*

Thanks to the adminstrative staff of the departement ***Katalin Bakóné Kósa, Ildikó Kerekes*** *and* ***Judit Csikós*** *for there continuous help.*

Thanks to all the members, colleagues and friends of the Departement of Solid – State Physics Faculty of science and Technology University of Debrecen. For there support and providing a warm work enviroment.

Thanks to the ***Stipendium Hungaricum scholarship board****,* ***Hungry****, and to the* ***Egyptian Ministry of Higher Education and Scientific Research****,* ***Egypt,*** *for giving me the opportunity to improve my academic and professional path. Thanks to* ***Prof. Dr/ Ola Abdelgawad, Dr/Anna Diltsch, Mr. Hatem Aly, Olaf Hahn*** *and all the members* ***Egypt's Office for Cultural and Educational Relations, Vienna****, for their continuous help and support.*

Thanks to my refrees for their efforts and insightful feedbacks and comments.

This work was supported by the National Research, Development and Innovation Office: NKFIH PD131784 project.

Despite the challenges posed by the COVID-19 pandemic, all the co-operations have pressed forward to pursuit the best opprtounities for my research activity.

Thanks to the kind people of Hungary whose hospitality provided me with beautiful, nice and affectionate experience. Special thanks to my supervisor kind family.

I am very greatful for the love, support and encouragement of my family and friends (Prof. Amina Youssef and Aya Bahaa). I dedicate this work to the memory of my beloved beloved father, who belived in me and has always been the source of my strength.